

Saturation of Stellar Winds from Young Suns

Takeru K. Suzuki¹, Shinsuke Imada^{2,4}, Ryuho Kataoka³, Yoshiaki Kato⁴, Takuma Matsumoto¹, Hiroko Miyahara⁵,
Saku Tsuneta⁴

stakeru@nagoya-u.jp

¹*Department of Physics, Nagoya University, Furo-cho, Chikusa, Nagoya, Aichi, 464-8602, Japan*

²*Solar-Terrestrial Environmental Laboratory, Nagoya University, Furo-cho, Chikusa, Nagoya, Aichi, 464-8601, Japan*

³*Interactive Research Center of Science, Tokyo Institute of Technology, 2-12-1 Ookayama, Meguro-ku, Tokyo, 152-8550 Japan*

⁴*Solar and Plasma Astrophysics Division, National Astronomical Observatory, 2-21-1, Osawa, Mitaka, Tokyo, 181-8588, Japan*

⁵*Institute for Cosmic Ray Research, The University of Tokyo, 5-1-5 Kashiwanoha, Kashiwa, Chiba 277-8582, Japan*

(Received ; accepted)

Abstract

We investigate mass losses via stellar winds from sun-like main sequence stars with a wide range of activity levels. We perform forward-type magnetohydrodynamical numerical experiments for Alfvén wave-driven stellar winds with a wide range of the input Poynting flux from the photosphere. Increasing the magnetic field strength and the turbulent velocity at the stellar photosphere from the current solar level, the mass loss rate rapidly increases at first owing to the suppression of the reflection of the Alfvén waves. The surface materials are lifted up by the magnetic pressure associated with the Alfvén waves, and the cool dense chromosphere is intermittently extended to 10 – 20 % of the stellar radius. The dense atmospheres enhance the radiative losses and eventually most of the input Poynting energy from the stellar surface escapes by the radiation. As a result, there is no more sufficient energy remained for the kinetic energy of the wind; the stellar wind saturates in very active stars, as observed in Wood et al. The saturation level is positively correlated with $B_{r,0}f_0$, where $B_{r,0}$ and f_0 are the magnetic field strength and the filling factor of open flux tubes at the photosphere. If $B_{r,0}f_0$ is relatively large $\gtrsim 5$ G, the mass loss rate could be as high as 1000 times. If such a strong mass loss lasts for ~ 1 billion years, the stellar mass itself is affected, which could be a solution to the faint young sun paradox. We derive a Reimers-type scaling relation that estimates the mass loss rate from the energetics consideration of our simulations. Finally, we derive the evolution of the mass loss rates, $\dot{M} \propto t^{-1.23}$, of our simulations, combining with an observed time evolution of X-ray flux from sun-like stars, which is shallower than $\dot{M} \propto t^{-2.33 \pm 0.55}$ in Wood et al.(2005).

Key words: magnetic fields – stars: coroneae – stars: late type – stars: mass loss – stars: winds, outflows – waves

1. Introduction

Main sequence stars with mass roughly below 1.5 solar mass (M_{\odot} hereafter) possess a surface convective layer, which is the main origin of X-ray and wind activities from such solar-type stars; magnetic fields are generated in a surface convective layer by dynamo mechanisms (e.g., Choudhuri et al.1995; Brun et al.2004; Hotta et al.2012) and turbulent motions associated with the magnetoconvection are the source to drive flares and outflows. Such magnetic activities are themselves interesting phenomena with fruitful physics, and in addition they may also affect planetary circumstances around central stars. Various researches have been carried out recently from this viewpoint (e.g., Terada et al.2009; Sterenborg et al.2011; Lammer et al.2012).

Young sun-like stars are very active: The observed X-ray flux is up to ~ 1000 times larger than the present solar level (Güdel et al. 1997; Güdel 2004), and the X-ray temperature is also higher (Ribas et al. 2005; Telleschi et al. 2005). There is an observational implication that a young star could have a very thick chromosphere extending to

10-20% of the stellar radius (Czesla et al. 2012), which is in contrast to the thin chromosphere of the present Sun with width of 0.1-1% of the solar radius (R_{\odot} hereafter). These observations show that in young sun-like stars the atmospheric materials are lifted up to higher altitudes and heated up more intensely in upper regions. This is probably related to the strong magnetic fields with an order of kG or even larger observed in young main sequence stars (Donati & Collier Cameron 1997; Saar & Brandenburg 1999; Saar 2001; see also Donati & Landstreet 2009 for recent review), which are much stronger than the average strength of 1-10 G of the present-day Sun.

On the other hand, the mass loss rates derived from the comparison between observations of near-by stars with the spectral types of G,K,M and spherical symmetric steady-state hydrodynamical simulations show a different trend (Wood et al.2002; 2005); after an increase of the mass loss rate with the increasing X-ray flux, it saturates at ~ 100 times of the current solar level and even drops in some very active stars. An explanation of the saturation is due to the change of the magnetic topology. It is expected that the surface area of active stars is mostly covered by closed

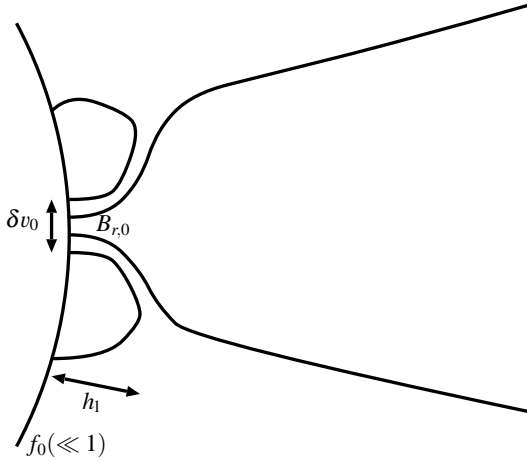


Fig. 1. Geometry of a flux tube and the input four parameters of the simulations. δv_0 is the velocity amplitude of open field lines at the photosphere. Magnetic field strength, $B_{r,0}$, at the photosphere, a filling factor, f_0 , of open flux tubes over the total photospheric surface, and a typical height, h_1 , of closed loops determine the properties of an open flux tube. h_1 corresponds to the location of the super-radial expansion of the flux tube. The combined variable, $(B_{r,0}f_0)$, determines the magnetic field strength in the outer region after the super-radial expansion finishes; $B_{r,0}f_0$ roughly corresponds to the large-scale field strength contributed from open flux tubes. As described later in this paper, δv_0 and $B_{r,0}f_0$ determine the energy injection from the photosphere, and h_1 affects the reflection of Alfvén waves in the chromosphere.

magnetic structure as a result of the strong magnetic fields (Schrijver & Aschwanden 2002). Then, the atmospheric gas is confined in closed loops rather than streaming out from open flux tubes (Wood et al. 2005; Vidotto et al. 2009).

In this paper, we propose an alternative and additional mechanism for the saturation. We focus on the dynamics in open magnetic flux tubes and show by numerical simulations that the saturation of the stellar winds could take place in open flux tube regions because of an enhancement of the radiative losses in active stars. The construction of the paper is as follows: After briefly introducing the setup of the MHD simulations in §2, we summarize in §3 basic formulations for the analysis of the wind energetics in the later sections. §4 presents the main results of the simulated stellar winds. In §5 we extensively discuss our results in light of observations of stellar winds (§5.1) and chromospheres (§5.3). In particular, we directly compare the simulated winds with the observations by Wood et al. (2002; 2005) in §5.1. In §5.2, we discuss the results in terms of the faint young Sun paradox.

2. Simulation Setup

2.1. Setup

We extend our one dimensional (1D) magnetohydrodynamical (MHD) simulation code originally developed for the present-day solar wind in Suzuki & Inutsuka (2005; 2006) to young active sun-like stars with strong magnetic

fields and large velocity fluctuations at the photosphere (§2.2). In this paper, we focus on main sequence stars and fix the basic stellar parameters on those of the present-day Sun, mass, $M = M_\odot$, radius, $r_0 = R_\odot$ and effective temperature, $T_{\text{eff}} = 5780$ K. Compared to the current Sun, the radius of a $1M_\odot$ star is slightly smaller by $\lesssim 10\%$ and the effective temperature also slightly lower within $\lesssim 200$ K at early epochs of the main sequence (Sackmann et al. 1993). However, we use the same radius and effective temperature in our simulations for both active and inactive stars because we would like to study responses of the stellar winds to the changes of the magnetic fields and velocity fluctuations at the photosphere¹.

We dynamically solve ideal MHD equations with radiative cooling and thermal conduction in super-radially expanding flux tubes from the photosphere with density, $\rho_0 = 10^{-7} \text{g cm}^{-3}$ (e.g. §9 of Gray 1992), and the sound speed $c_{s,0} = 6.31 \text{ km s}^{-1}$ (derived from $T_{\text{eff}} = 5780$ K) at $r = r_0$ to the outer boundary at $r \approx 30r_0$. We only consider the derivative with respect to r but treat the three components of velocity and magnetic field. We initially set up a static and cool ($T = 10^4$ K) atmosphere and start simulations by injecting the three components of velocity fluctuations from the photosphere with amplitude of each component, δv_0 ,

$$\langle \delta v_0^2 \rangle = \int_{\omega_{\min}}^{\omega_{\max}} P(\omega) d\omega, \quad (1)$$

where we adopt a frequency spectrum, $P(\omega) \propto \omega^{-1}$, from $1/\omega_{\max} = 20$ seconds to $1/\omega_{\min} = 30$ minutes. The normalization of $P(\omega)$ is determined to give δv_0 . Frequency spectrum of velocity perturbations have been observationally obtained by various instruments. Recent HINODE observation by Matsumoto & Kitai (2010), which obtained a frequency spectrum from 30 seconds to 70 minutes, shows a breaking power law with a flatter index = -0.6 in the lower frequency range, $1/\omega > 210$ seconds, and a steeper index = -2.4 in the higher frequency range. Our choice of $P(\omega) \propto \omega^{-1}$ is a reasonable fit to the observed spectrum with a single power law. For those who are interested in effects of different spectra, we would like to recall that Suzuki & Inutsuka (2006) performed the 1D MHD simulations with injected perturbations with white noise ($P(\omega) \propto \omega^0$) and monochromatic waves of frequency ω_0 ($P(\omega) \propto \delta(\omega - \omega_0)$).

Various modes of MHD waves are excited by the surface fluctuations (e.g. Isobe et al. 2008; Kato et al. 2011), and propagate upwardly (e.g., Bogdan et al. 2003; Okamoto & De Pontieu 2011). The Alfvén wave, among various modes, is supposed to play a major role in driving stellar winds mainly because it travels a long distance to the wind acceleration region (e.g., Alazraki & Couturier 1971; Hollweg 1973). A great advantage of the code is that we can determine mass loss rates as a direct output of the injected Poynting flux from the photosphere. Propagation,

¹ Also, such subtle changes of the radius and effective temperature give almost negligible effects on the dynamics and the energetics of the stellar winds.

reflection, and dissipation of these MHD waves are directly treated by the dynamical MHD simulations. We setup the spatially variable grids in order to resolve the Alfvén waves with the highest frequency ($1/\omega_{\max} = 20$ s.; shortest wavelength) we are injecting at least by $\gtrsim 10$ grid points everywhere. On the other hand, we cannot handle scales which are smaller than the grid scale and assume that sub-grid-scale structures are instantly transferred to the thermal energy by cascading processes or shocks to conserve the total energy equation. In our simulations, many shocklets form as a result of steepening of compressive waves which are nonlinearly generated from the propagating Alfvén waves (§3). These shocklets with the scales smaller than the grid scale are assumed to dissipate and heat up surrounding gas in our treatment.

As for the cooling in the coronal region, we adopt the cooling table for the optically thin plasma with the solar abundance (Landini & Monsignori-Fossi 1990; Sutherland & Dopita 1993), in which the cooling rate, q_R (erg $\text{cm}^{-3}\text{s}^{-1}$), is proportional to ρ^2 . For the cooling in the chromosphere, we adopt an empirical cooling rate $q_R = 4.5 \times 10^9 \rho \text{ erg cm}^{-3}\text{s}^{-1}$ by Anderson & Athay (1989). This cooling rate takes into account an effect of optically thick cooling under the non-LTE conditions (but see Carlsson & Leenaarts 2012 for a more detailed treatment based on snapshots of 2D MHD simulations). We smoothly connect the cooling rates in these two regimes by an interpolation. In the transition region, the cooling rate is initially $\propto \rho$ at lower heights but shifted to ρ^2 at higher altitudes.

We do not explicitly take into account stellar rotation in the dynamics of the stellar winds. If a star rotates by more than ~ 20 times faster than the present Sun, the terminal velocity of the wind will be affected (§5.5). However, the mass loss rate is affected little (Belcher & MacGregor 1976). The stellar rotation rather significantly affects the strengths of the generated magnetic fields (Holzwarth & Jardine 2007). In this paper, we consider this effect by incorporating wide ranges of the parameters on the magnetic fields.

2.2. Input Parameters

We investigate how the properties of the stellar winds depend on the following four parameters (Figure 1): Velocity perturbation, δv_0 , and radial magnetic field strength, $B_{r,0}$, a filling factor, f_0 , of open² flux tubes, which are all measured at the photosphere, and a typical height, h_1 , of closed loops, which surround an open flux tube we are considering. h_1 determines the location of the rapid expansion of a flux tube (Figure 1). From f_0 and h_1 , we adopt a functional form of a filling factor³ which depends on r ,

² We call an ‘open’ flux tube if the magnetic fields do not close in the simulation region.

³ In many literatures including ours (Suzuki & Inutsuka 2005; 2006) a super-radial expansion factor, instead of a filling factor, is used to set up open flux tubes. Defining $f'(r)$ as a super-radial expansion factor, these two factor are simply related as $f(r) = f_0 f'(r)$.

Label	$B_{r,0}f_0(\text{G})$	Label	$B_{r,0}(\text{kG})$
A	0.3125	a	0.5
B	0.625	b	1
C	1.25	c	2
D	2.5	d	4
E	5	e	8
F	10	f	16
Label	$\delta v_0(\text{km s}^{-1})$	Label	$h_1(/r_0)$
-2	0.669	α	0.01
0	1.34	β	0.03
+1	1.89	γ	0.1
+2	2.68		
+3	3.79		
+4	5.35		
+5	7.57		

Table 1. Labels for input parameters. For example, the label for the standard case is ‘Cb0 α ’.

$$f(r) = \frac{e^{\frac{r-r_0-h_1}{h_1}} + f_0 - (1-f_0)/e}{e^{\frac{r-r_0-h_1}{h_1}} + 1}. \quad (2)$$

This is the same functional form as in Kopp & Holzer (1976) with adopting $h_1 = R_1 - R_\odot = \sigma$ in Equation (11) of their paper. The conservation of magnetic flux fixes radial magnetic field,

$$B_r = B_{r,0} \frac{f_0 r_0^2}{f(r) r^2} \quad (3)$$

We would like to note that the combined variable, $(B_{r,0}f_0)$, determines the magnetic field strength in the outer region where the super-radial expansion already finishes, and corresponds to the field strength of larger-scale open flux tubes.

As a reference case for the present-day solar wind, we use the following values, which explain observed properties of polar coronal holes: $\delta v_0 = 1.34 \text{ km s}^{-1}$, $B_{r,0} = 1 \text{ kG}$, $f_0 = 1/800$, and $h_1 = 0.01 R_\odot (= 7 \times 10^3 \text{ km})$. The value of δv_0 is within the range of observed granulations (Holweger et al. 1978; Matsumoto & Kitai 2010). We adopt the values of $B_{r,0}$ and f_0 to explain recent observations by HINODE (Tsuneta et al. 2008; Shimojo & Tsuneta 2009; Ito et al. 2010; Shiota et al. 2012). In these papers, the authors reported that there are a number of super-radially open flux tubes anchored from strong magnetic field patches with $B_{r,0} \sim \text{kG}$ at the photosphere in polar regions. Comparing the photospheric magnetic field strength ($\sim 1 \text{ kG}$) and measured interplanetary field strengths normalized at the earth orbit ($\sim 1 - 10 \text{ nT} = 10^{-5} - 10^{-4} \text{ G}$; e.g., Smith & Balogh 2008), a typical filling factor, f_0 , of open field regions can be estimated as an order of 1/1000 (see Equation 3).

We perform 163 runs in wide ranges of the parameters: $\delta v_0 = (0.669 - 7.57) \text{ km s}^{-1}$, $B_{r,0} = (0.5 - 16) \text{ kG}$, $f_0 = (1/400 - 1/6400)$, and $h_1 = (0.01 - 0.1)r_0$. Compared with the parameters for the present-sun case just described above, we consider more cases with larger δv_0 , larger $B_{r,0}$, smaller f_0 , and larger h_1 . We naively expect that δv_0 is larger in active stars, whereas too strong magnetic fields might inhibit footpoint motions of flux tubes

(Katsukawa & Tsuneta 2005). Since the actual δv_0 is quite uncertain observationally, we adopt the wide range $\delta v_0 = 0.669 - 7.57 \text{ km s}^{-1}$, from $\sim 10\%$ of the sound speed ($= 6.31 \text{ km s}^{-1}$) to a moderately super-sonic regime at the photosphere. The photospheric magnetic field strengths, $B_{r,0}$, of active stars are expected to be larger than that of the present solar (*e.g.*, Donati et al. 2009). We should note that $B_{r,0}$ does not coincide with large-scale magnetic field strengths observed in solar-type stars (*e.g.*, Figure 3 of Donati et al. 2009), which will be discussed in more detail in §5.1.2. The large-scale field strength contributed from open flux tubes roughly corresponds to $B_{r,0}f_0$. In addition, the contribution from large-scale closed magnetic loops should be taken into account in order to estimate the total large-scale magnetic field strength. In this context, a filling factor, f_0 , of open flux tubes is also an important parameter. At the same time, however, it is quite difficult to observationally determine typical f_0 of stars except for the sun. During the solar maximum of the present-day sun, a larger fraction of the surface is covered by closed structures (Hakamada et al. 2005), which implies f_0 is smaller. The magnetic states of active stars are considered to be a more extreme state of the solar maximum, and hence, we infer that f_0 of active stars is smaller. Thus, we consider the larger number of cases with smaller f_0 . A typical height, h_1 , of closed loops of some active stars can be inferred from stellar flares through the RTV scaling law (Rosner et al. 1978). Shibata & Yokoyama (1999) derived a scaling relation for solar and stellar flares showing that the loop lengths of active stars are longer than those of the present sun.

We label the simulated models by (A – F) for $B_{r,0}f_0$, (a – f) for $B_{r,0}$, ($-2 - +5$) for δv_0 , and ($\alpha - \gamma$) for h_1 , which are tabulated⁴ in Table 1. Using these labels, for instance the standard case ($B_{r,0}f_0 = 1.25 \text{ G}$, $B_{r,0} = 1 \text{ kG}$, $\delta v_0 = 1.34 \text{ km s}^{-1}$, and $h_1 = 0.01r_0$) is labeled as ‘Cb0 α ’.

3. Energetics Formulation

In this paper, we investigate how the mass losses are controlled by the surface properties by examining the energetics of the simulated stellar winds. We firstly consider the time-averaged structure of each simulation run in the next section (§4). In this section we summarize some basic equations for the wind energetics. Under the steady state conditions, an equation of the total energy can be written as (*e.g.*, Fisk et al. 1999; Suzuki 2006)

$$\begin{aligned} \nabla \cdot \left[\rho \mathbf{v} \left(\frac{v^2}{2} + \frac{\gamma}{\gamma-1} \frac{p}{\rho} - \frac{GM}{r} \right) \right. \\ \left. - \frac{1}{4\pi} (\mathbf{v} \times \mathbf{B}) \times \mathbf{B} + \mathbf{F}_c \right] + q_R = 0, \end{aligned} \quad (4)$$

where \mathbf{F}_c is thermal conductive flux, and the other variables have the conventional meanings. We focus on the

radial component of the equation from now. We can write the divergence of an arbitrary vector, \mathbf{A} , as

$$\nabla \cdot \mathbf{A} = \frac{1}{r^2 f} \frac{\partial}{\partial r} (r^2 f A_r) \quad (5)$$

to take into account the super-radial expansion of an open flux tube. The integration of Equation (4) from an arbitrary reference point, r_{ref} , to r gives

$$\begin{aligned} 4\pi r^2 f \left[\rho v_r \left(\frac{v^2}{2} + \frac{\gamma}{\gamma-1} \frac{p}{\rho} - \frac{GM}{r} \right) + v_r \frac{B_\perp^2}{4\pi} \right. \\ \left. - B_r \frac{v_\perp B_\perp}{4\pi} + F_{c,r} \right] + 4\pi \int_{r_{\text{ref}}}^r q_R r^2 f dr \\ = \dot{M} \left(\frac{v^2}{2} + \frac{\gamma}{\gamma-1} \frac{p}{\rho} + \frac{B_\perp^2}{4\pi\rho} - \frac{GM}{r} \right) \\ - \Phi_B \frac{v_\perp B_\perp}{4\pi} + 4\pi r^2 f F_{c,r} + 4\pi \int_{r_{\text{ref}}}^r q_R r^2 f dr = \text{const.}, \end{aligned} \quad (6)$$

where subscript, \perp , indicates the perpendicular components to the radial direction, \dot{M} is mass loss rate,

$$\dot{M} = 4\pi r^2 f \rho v_r, \quad (7)$$

and Φ_B is radial magnetic flux,

$$\Phi_B = 4\pi r^2 f B_r. \quad (8)$$

The energy flux of Alfvén waves along with r direction can be written as

$$F_A = v_r \left(\rho \frac{v_\perp^2}{2} + \frac{B_\perp^2}{4\pi} \right) - B_r \frac{v_\perp B_\perp}{4\pi}, \quad (9)$$

(Jacques 1977; Cranmer et al. 2007). One may notice that F_A partly consists of Equation (6). Integrating over the total area of the open flux tubes on a stellar surface, we can define Alfvén wave luminosity, L_A , as

$$\begin{aligned} L_A(r) f(r) &= 4\pi r^2 f(r) F_A(r) \\ &= \dot{M} \left(\frac{v_\perp^2}{2} + \frac{B_\perp^2}{4\pi\rho} \right) - \Phi_B \frac{v_\perp B_\perp}{4\pi}. \end{aligned} \quad (10)$$

Since we consider the energy transfer in super-radially open flux tubes, luminosity, $L_A f$, from open flux tubes, instead of L_A integrated over the total area, should be treated in the energy conservation.

The right-hand side of Equation (9) is separated into the two parts; the first term indicates the energy flux advected by background flow, v_r , and the second term, which exists even in static media, is the Poynting flux involving magnetic tension. We can introduce Elsässer variables,

$$z_\pm = v_\perp \mp \frac{B_\perp}{\sqrt{4\pi\rho}}, \quad (11)$$

where z_+ (z_-) denotes an amplitude of Alfvén waves which travels to the (anti-)parallel direction with B_r . Using z_\pm , the second term of Equation (9) can be expressed as

$$-B_r \frac{v_\perp B_\perp}{4\pi} = \frac{1}{4} \rho (z_+^2 - z_-^2) v_A, \quad (12)$$

⁴ The labels for δv_0 are the twice of the power-law indices of 2 scaled by $\delta v_0 = 1.34 \text{ km s}^{-1}$ of the standard case. For example, ‘+3’ for $\delta v_0 = 3.79 \text{ km s}^{-1}$ is from $(3.79\dots)^2 = 2^{+3} \times (1.34\dots)^2$ or $3.79\dots = 2^{+3/2} \times 1.34\dots$.

where $v_A = \frac{B_r}{\sqrt{4\pi\rho}}$ is Alfvén velocity. This expression illustrates that $\frac{1}{4}\rho z_+^2$ ($\frac{1}{4}\rho z_-^2$) corresponds to the energy density of Alfvén waves to the (anti-)parallel direction with B_r , and that $-B_r \frac{v_r B_r}{4\pi}$ corresponds to the net positively traveling (parallel with B_r) Poynting flux associated with Alfvén waves in static media.

After the injection of Alfvén waves from the photosphere $L_A f$ decreases because of various types of damping processes, such as turbulent cascade (Matthaus et al. 1999; Chandran 2005; Cranmer et al. 2007; Verdini & Velli 2007), phase mixing (Heyvaerts & Priest 1983; Grappin et al. 2000; De Moortel et al. 2000), nonlinear mode conversion to compressive waves by magnetic pressure, $B_\perp^2/8\pi$ (ponderomotive force; Kudoh & Shibata 1999; Suzuki & Inutsuka 2005; 2006) and by parametric decay (Goldstein 1978; Terasawa et al. 1986; Suzuki & Inutsuka 2006; Nariyuki 2009), ioncyclotron resonance (e.g., Axford & McKenzie 1997; Tu & Marsch 2001). Because of the 1D MHD approximation our simulations cannot take into account all these processes but mainly consider the nonlinear mode conversion to compressive waves by the ponderomotive force and parametric decay. However, our simulations are calibrated to reproduce the current solar wind, namely this can give a reasonable heating profile at least for the solar wind observed today although 3D and/or kinetic effects which we do not cover might play a role in the actual wave dissipation. We extend the calibrated case to extreme conditions for young suns. Recently, Matsumoto & Suzuki (2012) have performed 2D MHD simulations, which can handle phase mixing and a part of turbulent cascade in addition to the nonlinear generation of compressive waves. Interestingly, the 1D (Suzuki & Inutsuka 2005; Suzuki & Inutsuka 2006) and the 2D (Matsumoto & Suzuki 2012) simulations give the similar wind structures for the present-day solar wind although the dissipation channels are different. In future works, we extend the 2D MHD simulation to the conditions for young active suns.

After the damping of the Alfvén waves, a small fraction of the input energy is finally transferred to the kinetic energy of stellar winds,

$$L_K(r)f(r) = \dot{M} \frac{v_r^2}{2} = 4\pi r^2 f(r) \rho v_r \frac{v_r^2}{2} = 4\pi r^2 f(r) F_K(r), \quad (13)$$

where F_K and L_K are kinetic energy flux and luminosity.

Our main aim is to understand how the wind kinetic energy luminosity, $L_K(r_{\text{out}})f(r_{\text{out}}) = L_K(r_{\text{out}})$ (note $f(r_{\text{out}}) = 1$), at the outer boundary, $r_{\text{out}} \approx 30r_0$, is determined by the input Poynting flux $(L_A f)_0$ at the photosphere. Hereafter, we express, e.g. $(L_A f)_0$ and $L_{K,\text{out}}$, etc. for $L_A(r_0)f_0$ and $L_K(r_{\text{out}})$ for simplicity. In our simulations, we only inject velocity perturbations with δv_0 from the photosphere without magnetic field perturbation. Then, the input energy flux can be written as $F_{A,0} = \rho_0 \langle \delta v_0^2 \rangle v_{A,0}$ in the static background ($v_r = 0$), where $\langle \delta v_0^2 \rangle$ is kinetic energy per mass of the sum of the two transverse components. Then, the input wave luminosity is

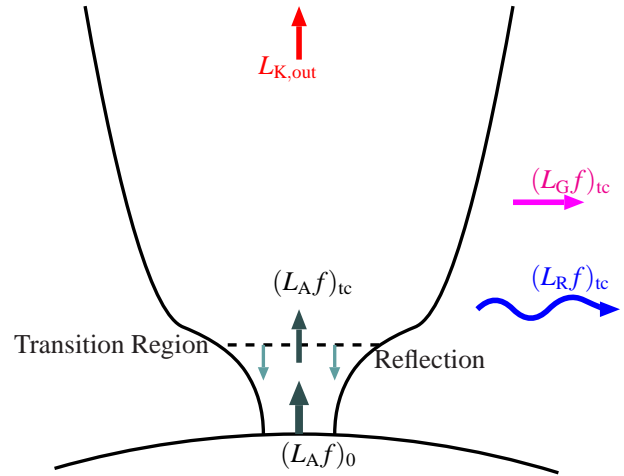


Fig. 2. Schematic picture for the energetics in an open flux tube. Please see *text* for the notation of each variable.

$$(L_A f)_0 = 4\pi r_0^2 f_0 \rho_0 \langle \delta v_0^2 \rangle v_{A,0}. \quad (14)$$

We examine the energetics of the stellar winds by two steps (Figure 2); we firstly inspect the energetics in the chromospheres. Here, the reflection of outgoing Alfvén waves play an important role because the Alfvén speeds change rapidly because of the steep decrease of the densities. We define $r = r_{\text{tc}}$ as the top of the chromosphere where $T = 2 \times 10^4$ K. The density, ρ_{tc} , at $r = r_{\text{tc}}$ is determined by the energy balance among the heating by wave dissipation, the downward thermal conduction, and the radiative cooling in the transition region (Rosner et al. 1978). For larger heating, ρ_{tc} is larger because of the larger chromospheric evaporation through the downward thermal conduction as a result of the larger heating in the corona. We measure $(L_A f)_{\text{tc}}$ at $r = r_{\text{tc}}$ to quantify the reflection (§4.2), and inspect the transmissivity,

$$c_T = (L_A f)_{\text{tc}} / (L_A f)_0, \quad (15)$$

of the Alfvén waves through the chromosphere in different cases.

Next, we examine how much fraction of the surviving wave energy, $(L_A f)_{\text{tc}}$, is finally transferred to the wind kinetic energy (§4.2.2). By comparing dominant terms at r_{tc} and at r_{out} in Equation (6), we can derive an energy conservation relation:

$$L_{K,\text{out}} \approx (L_A f)_{\text{tc}} - (L_R f)_{\text{tc}} - (L_G f)_{\text{tc}}, \quad (16)$$

where

$$(L_R f)_{\text{tc}} \equiv 4\pi \int_{r_{\text{tc}}}^{r_{\text{out}}} q_R r^2 f dr \quad (17)$$

is the radiation loss from $r = r_{\text{tc}}$ to the outer region, and the gravitational loss,

$$(L_G f)_{\text{tc}} \equiv \dot{M} \frac{GM}{r_{\text{tc}}}. \quad (18)$$

Please note that the energy loss by the downward thermal conduction in the transition regions is included in the radiation loss term, $(L_R f)_{\text{tc}}$, because the thermal conduc-

tive flux from the upper coronae mainly escapes by the radiation in the transition regions (Rosner et al. 1978). As explained previously in this section, the density, ρ_{tc} , at r_{tc} , which corresponds to the ‘base’ density for stellar winds, is determined by this energy balance.

4. Results

4.1. Photosphere – Wind connection

Before carrying out detailed analyses, we show the relation between the input Alfvén wave luminosity $(L_A f)_0$ from the photosphere and the output kinetic energy, $L_{K,out}$. The top panel of Figure 3 shows the $(L_A f)_0 - L_{K,out}$ diagram. In the figure we overplot three lines for constant conversion factors, $c_E = 0.001, 0.01, 0.1$, from $(L_A f)_0$ to $L_{K,out}$ by the three lines. Using Equations (3) and (14) with $v_{A,0} = B_{r,0}/\sqrt{4\pi\rho_0}$, we can explicitly write the relation that connects $L_{K,out}$ to $(L_A f)_0$:

$$\begin{aligned} L_{K,out} &= c_E (L_A f)_0 = c_E \Phi_B \sqrt{\frac{\rho_0}{4\pi}} \langle \delta v_0^2 \rangle \\ &= 2.1 \times 10^{27} \text{erg s}^{-1} \left(\frac{c_E}{0.017} \right) \\ &\quad \left(\frac{B_{r,0} f_0}{1.25 \text{G}} \right) \left\langle \left(\frac{\delta v_0}{1.34 \text{km s}^{-1}} \right)^2 \right\rangle, \end{aligned} \quad (19)$$

where we already substitute $r_0 = R_\odot$ and $\rho_0 = 10^{-7} \text{g cm}^{-3}$ adopted in the simulations. We discuss a more general expression for stars with different radius and photospheric density in §5.4. The relation is normalized by the input parameters and the output $L_{K,out} = 2.1 \times 10^{27} \text{erg s}^{-1}$ with $c_E = 0.017$ of the standard case for the present-day solar wind (Model Cb0 α). Among the four input parameters, the dependence on $B_{r,0}$, f_0 , and δv_0 is explicitly shown in Equation (19), but h_1 does not appear because h_1 causes variations of c_E (vertical scatters of L_K in the panel).

Different symbols (& colors) are used for different sets of $B_{r,0} f_0$ in Figure 3. We would like to note that $B_{r,0} f_0$ determines the magnetic field strength in the outer region where the super-radial expansion of the flux tubes is already completed ($f(r) \rightarrow 1$ in Equation 3). $B_{r,0} f_0$ is a good indicator of the properties of the solar wind, particularly the wind speed (Kojima et al. 2005; Suzuki et al. 2006). The figure shows that the conversion factor is distributed in a range of $0.001 < c_E < 0.1$, and a typical value is $c_E \sim 0.01$.

Although there are scatters, focusing on a single set of $B_{r,0} f_0$ (*i.e.* data points with a same symbol and color), c_E shows a rather clear trend which is not monotonic; c_E initially increases, namely $L_{K,out}$ increases with $(L_A f)_0$ much faster than the linear, which is followed by a decrease of c_E or a saturation (or even decrease) of $L_{K,out}$ in the large $(L_A f)_0$. The initial increase of c_E can be explained by the suppression of the reflection of the Alfvén waves (Suzuki 2012), which we discuss in §4.2. The later decrease is due to the enhanced radiative losses (§4.3). The figure shows that the saturation level of $L_{K,out}$ is determined by $B_{r,0} f_0$, which we also discuss in §4.3.

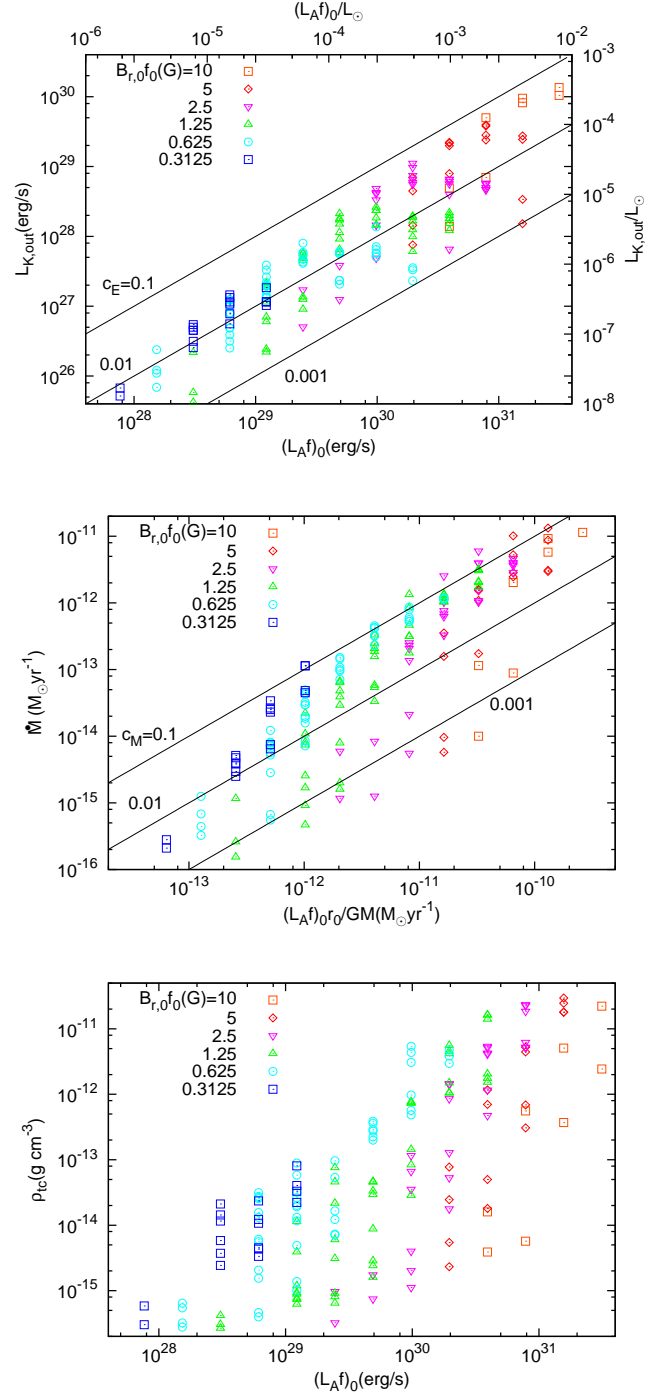


Fig. 3. *top:* Relation between the final kinetic energy luminosity, $L_{K,out}$, and the input wave energy luminosity, $(L_A f)_0$, at the photosphere of the simulated stellar winds. The lines indicate constant conversion factors, $c_E = 0.1, 0.01, 0.001$. The right and top axes are normalized by the solar luminosity, $L_\odot = 4 \times 10^{33} \text{erg s}^{-1}$. *middle:* Relation between \dot{M} and $(L_A f)_0$ divided by $\frac{v_{esc,0}^2}{2} = \frac{GM}{r_0}$. The lines indicate constant conversion factors, $c_M = 0.1, 0.01, 0.001$. *bottom:* Relation between the density, ρ_{tc} , at the top of the chromosphere and $(L_A f)_0$.

Focusing on a single set of $B_{r,0}f_0$ (a same symbol and color), if we input further larger δv_0 to increase $(L_A f)_0$, $L_{k,out}$ will be smaller to give $c_E < 0.001$ and to fill the lower right corner of the panel. However, the largest $\delta v_0 = 7.57$ km s⁻¹ is already supersonic driving at the photosphere (note $c_{s,0} = 6.31$ km s⁻¹), which is probably extremely large. Therefore, we can conclude that the conversion factor is located well in the range of $0.001 < c_E < 0.1$ in the realistic situations.

The top panel of Figure 3 also shows vertical scatters. This indicates that the final wind kinetic energies are different even though the input $(L_A f)_0 (\propto B_{r,0}f_0 \delta v_0^2)$'s are identical. This is mainly because of the difference of h_1 , which controls the reflection and transmission of the Alfvén waves in the chromosphere, which we will discuss in §4.2.

It is more useful for readers to show the mass loss rates as a function of surface properties. The middle panel of Figure 3 shows \dot{M} with wave luminosity divided by $\frac{v_{esc,0}^2}{2} = \frac{GM}{r_0}$ in order that both axes are in unit of $M_\odot \text{yr}^{-1}$, where $v_{esc,0} (= 618$ km s⁻¹) is the escape velocity. Similarly to the scaling relation for $L_{K,out}$ (Equation 19), we can define a conversion factor, c_M , with respect to the mass loss rates, and then, we have

$$\begin{aligned} \dot{M} &= c_M \frac{(L_A f)_0 r_0}{GM} = c_M \Phi_B \sqrt{\frac{\rho_0}{4\pi}} \frac{\langle \delta v_0^2 \rangle r_0}{GM}, \\ &= 2.2 \times 10^{-14} M_\odot \text{yr}^{-1} \left(\frac{c_M}{0.023} \right) \\ &\quad \left(\frac{B_{r,0}f_0}{1.25G} \right) \left\langle \left(\frac{\delta v_0}{1.34 \text{ km s}^{-1}} \right)^2 \right\rangle \end{aligned} \quad (20)$$

where we already substitute $M = M_\odot$, $r_0 = R_\odot$, and $\rho_0 = 10^{-7}$ g cm⁻³ that are adopted in the simulations, but see §5.4 for a more general expression. Here, the normalizations are again adopted from the input parameters and the results ($\dot{M} = 2.2 \times 10^{-14} M_\odot \text{yr}^{-1}$ and $c_M = 0.023$) of the standard case for the present-day Sun.

In the bottom panel of Figure 3, we plot the density, ρ_{tc} , at the top of the chromosphere defined at $T = 2 \times 10^4$ K. ρ_{tc} , which essentially corresponds to the so-called base density for the stellar winds, is determined by the energy balance among the wave heating in the above corona, the downward thermal conduction, and the radiative cooling in the transition region as described in §3. A larger energy injection, $(L_A f)_0$, from the photosphere leads to larger heating in the corona. Then, the downward thermal conduction from the corona is enhanced, which increases ρ_{tc} by the chromospheric evaporation. Comparison of the bottom panel to the top and middle panels show that the differences of $L_{K,out}$ and \dot{M} that extent more than orders of magnitude among different cases can be mainly explained by the differences of ρ_{tc} . Moreover, the scatters of $L_{K,out}$ on a fixed $(L_A f)_0$ are smaller than the scatters of ρ_{tc} . This is mainly because the wind speed becomes slower as the wind density ($\propto \rho_{tc}$) increases with increasing $(L_A f)_0$; the dense wind cannot be accelerated to high speed. Related to this, the top panel of Figure 3 illustrates

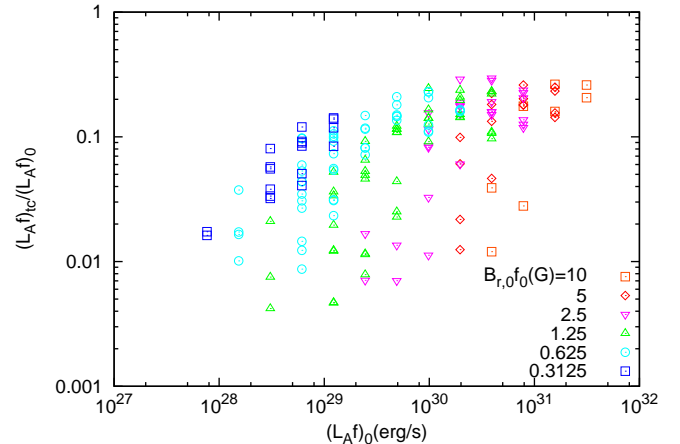


Fig. 4. Surviving fraction, $c_T = (L_A f)_{tc} / (L_A f)_0$, of the Alfvén wave luminosity at the top of the chromosphere versus input wave luminosity at the photosphere, $(L_A f)_0$.

that the average trend of c_E does not show a systematic trend with $(L_A f)_0$, while the middle panel still shows that the average trend of c_M is slightly increasing with $\frac{(L_A f)_0 r_0}{GM}$. However, this issue needs a caution. If a star rotates very rapidly, the wind speed of active cases (on the right side of the panels) might be higher. In this case c_E might show an increasing trend with $(L_A f)_0$, similarly to c_M .

4.2. Initial Increase of $L_{K,out}$ - Wave Reflection -

4.2.1. Energetics

A sizable fraction of the input Alfvén waves suffers reflection before reaching the corona (Hollweg 1984; Moore et al. 1991; Murawski & Musielak 2010; Verdini, Grappin, & Velli 2012). Observation by HINODE obtained signatures of reflected Alfvén waves at the photosphere (Fujimura & Tsuneta 2009). In the chromosphere, the density decreases very rapidly, which leads to the rapid increase of the Alfvén velocity. Therefore, the shape of outwardly propagating Alfvén waves is considerably deformed, which indicates that these waves are reflected back downward. For the current solar condition, typically $\gtrsim 90$ % of the input energy is reflected back downward (Suzuki & Inutsuka 2006; Matsumoto & Suzuki 2012).

We measure $(L_A f)_{tc}$ at the top of the chromospheres, $r = r_{tc}$, to quantitatively study the surviving fractions ($= c_T$ in Equation 15) after the propagation through the chromospheres. The reflected waves are mostly dissipate through the downward propagation in the chromospheres and finally lost by the radiation, where some fractions are considered to be again reflected upward and may be trapped (Matsumoto & Shibata 2010). Therefore, the radiation loss in the chromospheres is mostly taken into account in the component of the reflected waves.

Figure 4 displays $c_T = (L_A f)_{tc} / (L_A f)_0$. For small $(L_A f)_0$, the reflection of the Alfvén waves is so effective that only $\sim 1\%$ of the input energies can transit through the chromospheres. On the other hand, the fraction is in-

Model	δv_0	$B_{r,0}(\text{kG}) \times f_0$	$h_1 (r_0)$	$(L_A f)_0$	$(L_A f)_{tc}$	c_T	$M (M_\odot \text{yr}^{-1})$	$v_{r,\text{out}}$	$L_{K,\text{out}}$	$(L_R f)_{tc}$
Cb0 α	1.34	1/800	0.01	1.2×10^{29}	6.4×10^{27}	0.052	2.2×10^{-14}	554	2.1×10^{27}	1.5×10^{27}
Cc-2 β	0.669	2/1600	0.03	3.1×10^{28}	1.3×10^{26}	0.0042	1.5×10^{-16}	932	4.2×10^{25}	1.2×10^{25}
Cc0 β	1.34	2/1600	0.03	1.2×10^{29}	1.5×10^{27}	0.012	2.5×10^{-15}	933	7.0×10^{26}	4.8×10^{25}
Cc+2 β	2.68	2/1600	0.03	4.9×10^{29}	5.7×10^{28}	0.12	2.5×10^{-13}	438	1.5×10^{28}	9.2×10^{27}
Cc+4 β	5.35	2/1600	0.03	2.0×10^{30}	3.0×10^{29}	0.15	1.1×10^{-12}	239	1.9×10^{28}	3.8×10^{29}

Table 2. Input parameters and outputs for the cases shown in Figures 5 & 7. The unit of δv_0 and $v_{r,\text{out}}$ is km s^{-1} , and the unit of L is erg s^{-1} . c_T is the transmission fraction of the Alfvén waves from the photosphere to the top of the chromosphere (Equation 15). Model Cb0 α is the reference case for the present sun, and the lower four Models are the cases with different δv_0 by twice each but with the same $B_{r,0}f_0$ and h_1 .

creasing with increasing $(L_A f)_0$ and finally reaches ~ 0.3 . This trend can be understood from the density structures in the chromospheres, which is discussed later (Fig.5). In short, in cases with large energy inputs the reflection of the outgoing Alfvén waves is not so effective because the densities decrease more slowly and accordingly the change of the Alfvén speeds is more gradual.

The suppression of the reflection of the Alfvén waves (the increase of c_T with $(L_A f)_0$) is the main reason of the initial rise of the energy conversion factor, $c_E (= L_{K,\text{out}}/(L_A f)_0$; Equation 19) shown in Fig.3. A larger fraction of the Alfvén waves transmits to upper regions, which directly leads to the larger final kinetic energy of the stellar wind.

Figure 4 also shows that c_T largely scatters even for the same sets of δv_0 and $B_{r,0}f_0$ (same symbol and color at same $(L_A f)_0$) because of the effect of different h_1 . Larger h_1 indicates that the magnetic field strength in the chromospheric region is larger, and the Alfvén speed more rapidly increases due to the decrease of the density. As a result, a larger fraction of the Alfvén waves from the photosphere is reflected back, giving smaller c_T .

4.2.2. Atmospheric Structure

We demonstrate simulated wind structures with different energy inputs. In Figure 5, we plot the time-averaged structures of the four cases with the same $B_{r,0}f_0 = 2(\text{kG})/1600$ and $h_1 = 0.03r_0$ but different δv_0 by twice each in comparison with the case for the present sun (Table 2). The input energy of the four cases is different by four times each since $(L_A f)_0 \propto B_{r,0}f_0 \delta v_0^2$.

The top panel of Figure 5 indicates that the decrease of the density becomes slower with increasing the energy input from the surface. This is mainly because in the active cases the magnetic pressure dominantly supports the chromospheric density structure in addition to the gas pressure. Figure 6 compares the force (per mass) by the magnetic pressure gradient (solid lines) with the force by the gas pressure gradient (dashed lines) of the most inactive case (Model Cc-2 β ; left panel, corresponding to the black dotted lines in Figure 5) and the most active case (Model Cc+4 β ; right panel, corresponding to the blue dot-dashed lines in Figure 5) in Table 2. The left panel shows that in the inactive case the gas pressure gradient dominates in the chromosphere and the transition region, $r - r_0 < 10^{-2}r_0$. On the other hand, in the active case (right panel) the magnetic pressure gradient dominantly supports the density structure at and above

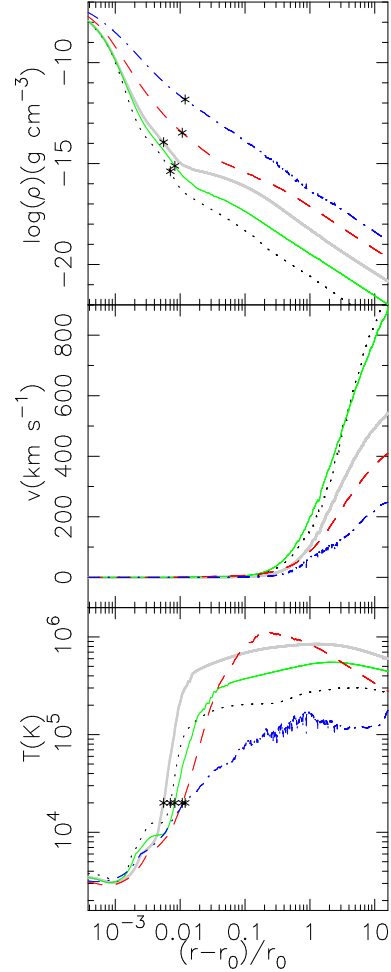


Fig. 5. Comparison of the time-averaged wind structures in Table 2. The four cases with the same $B_{r,0}f_0 = 2(\text{kG})/1600$ and $h_1 = 0.03r_0$ but different δv_0 by twice each (Cc-2 β : black dotted, Cc0 β : green solid, Cc+2 β : red dashed, and Cc+4 β : blue dot-dashed) are compared with the reference case for the present sun (Cb0 α : thick gray solid). From top to bottom, the densities, radial velocities, and temperatures are compared. In the top and bottom panels, the location of the top of the chromosphere at $T = 2 \times 10^4$ K of each case is shown by asterisks.

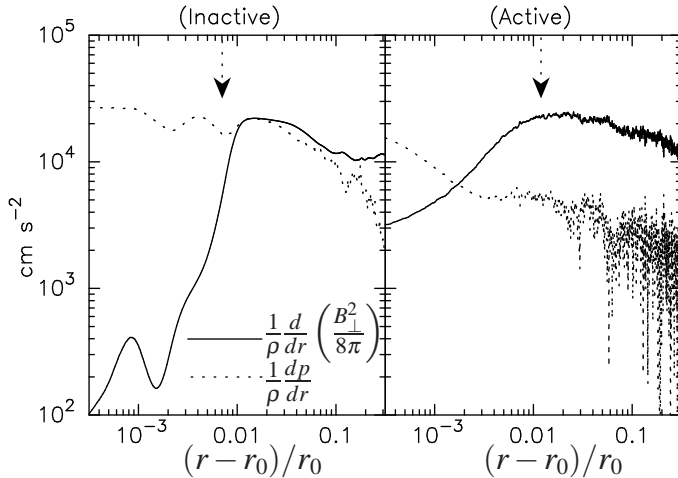


Fig. 6. Comparison of the accelerations (forces per mass) by the magnetic pressure gradient (solid lines) and the gas pressure gradient (dashed lines) of the most inactive case (Model Cc-2 β ; left) and the most active case (Model Cc+4 β ; right) in Table 2. The location of the top of the chromosphere at $T = 2 \times 10^4$ K is also shown by the vertical arrow in each panel.

the middle chromosphere, $r - r_0 > 2 \times 10^{-3} r_0$, because the input wave amplitude ($\delta v_{\perp} \propto \delta B_{\perp}$) from the surface itself is larger. As a result, the cool chromospheric material extends to an upper region. The density of the upper region is also larger, which leads to the larger \dot{M} .

The change of the density structure directly affects the reflection of the Alfvén waves. In the chromosphere the Alfvén speed, $v_A = B_r / \sqrt{4\pi\rho}$, generally increases with height because of the decrease of the density. The slower decrease of the density in the active case makes the change of v_A more gradual. Then, the reflection of the Alfvén waves is not so severe in the active case, which we will discuss in §4.2.3 and Figure 7. Table 2 clearly indicates that the transmissivity ($c_T = (L_A f)_{tc} / (L_A f)_0$) of the Alfvén waves through the chromosphere increases with the input energy as shown in Figure 4. Accordingly, the kinetic energy luminosity, $L_{K,out}$, and the mass loss rate, \dot{M} , rapidly increase with $(L_A f)_0$. The radiation loss, $(L_R f)_{tc}$, also rapidly increases with $(L_A f)_0$, and its dependence is faster than the dependence of $L_{K,out}$, which we discuss in §4.3 in terms of the saturation of the stellar winds.

The middle panel of Figure 5 shows that the wind velocity becomes slower with increasing the energy input because more mass is lifted up to the wind region, and then, the wind material cannot be effectively accelerated to higher velocities.

The bottom panel of Figure 5 indicates that the maximum temperature increases with increasing the input energy up to the second most active case with $\delta v_0 = 2.68$ km s $^{-1}$ (Model Cc+2 β ; red dashed). On the other hand, in the most active case with $\delta v_0 = 5.35$ km s $^{-1}$ (Model Cc+4 β ; blue dot-dashed) the temperature is low with-

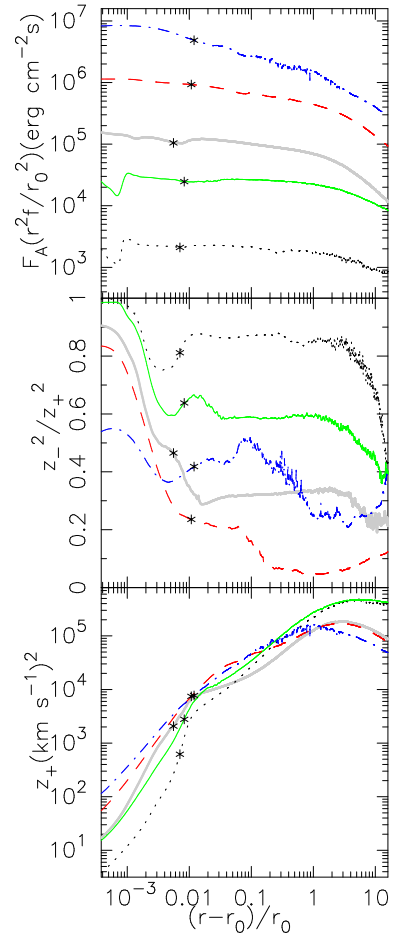


Fig. 7. Comparison of time-average Alfvén wave properties of the three cases tabulated in Table 2. The line types are the same as in Figure 5. The reference case for the current sun is shown (Model Cb0 α ; thick gray solid) in comparison, and the other four cases adopt the different input Poynting flux, $(L_A f)_0$, from the photosphere by 4 times each. The location of the top of the chromosphere at $T = 2 \times 10^4$ K of each case is shown by asterisks. *top*: Energy flux of the Alfvén waves. In order to remove the effect of the expansion of the flux tubes, we display $F_A r^2 f / r_0^2 = L_A f / 4\pi r_0^2$ (see Equation 9 or 11), *middle*: Ratio of the outgoing and incoming (reflected) components of the Alfvén waves, z_-^2 / z_+^2 . *Bottom*: Squared Elsässer variable, z_+^2 .

out the steady hot corona with $T \gtrsim 10^6$ K, because the radiative cooling ($\propto \rho^2$ in the optically thin plasma) is efficient in the dense circumstances. As a result, the coronal temperature cannot be maintained, and the temperature time-dependently goes up and down from $\sim 10^4$ K to $\gtrsim 10^6$ K (§5.3) because of the thermal instability in the radiative cooling function (Sutherland & Dopita 1993; Suzuki 2007). The plotted value of temperature, $\sim 10^5$ K, is the time-averaged value.

The temperature of the second most active case still drops faster than the cases with smaller δv_0 because the thermal conduction is relatively ineffective in comparison with the adiabatic cooling in the high density circumstances.

Model	δv_0	$B_{r,0}(\text{kG}) \times f_0$	$h_1(r_0)$	$(L_A f)_0$	$(L_A f)_{tc}$	c_T	$\dot{M} (M_\odot \text{yr}^{-1})$	$v_{r,\text{out}}$	$L_{K,\text{out}}$	$(L_R f)_{tc}$
Ac+2 γ	2.68	2/6400	0.1	1.2×10^{29}	1.7×10^{28}	0.14	1.1×10^{-13}	226	1.8×10^{27}	2.4×10^{27}
Bc+4 β	5.35	2/3200	0.03	9.8×10^{29}	1.1×10^{29}	0.11	5.6×10^{-13}	278	1.4×10^{28}	1.8×10^{29}
Cd+3 γ	3.79	4/3200	0.1	9.8×10^{29}	1.6×10^{29}	0.17	8.5×10^{-13}	313	2.6×10^{28}	2.2×10^{28}
Df+3 γ	3.79	16/6400	0.1	2.0×10^{30}	5.7×10^{29}	0.29	2.5×10^{-12}	373	1.1×10^{29}	7.2×10^{28}
Ef+4 γ	5.35	16/3200	0.1	7.8×10^{30}	2.1×10^{30}	0.26	1.0×10^{-11}	351	3.9×10^{29}	4.5×10^{29}
Ff+5 γ	7.57	16/1600	0.1	3.1×10^{31}	8.2×10^{30}	0.26	4.3×10^{-11}	317	1.4×10^{30}	2.9×10^{30}

Table 3. Saturated cases for $B_{r,0}f_0 = 0.3125, 0.625, 1.25, 2.5, 5, 10(\text{G})$ from top to bottom, shown in Figure 10. The unit of δv_0 and $v_{r,\text{out}}$ is km s^{-1} , and the unit of L is erg s^{-1} . c_T is the surviving fraction of the Alfvén waves from the photosphere to the top of the chromosphere (Equation 15).

4.2.3. Wave Properties

Figure 7 displays properties of the Alfvén waves of the same cases shown in Figure 5 and Table 2. The top panel of Figure 7 compares the Alfvén wave energy fluxes (Equation 9). Here we plot $F_A r^2 f / r_0^2 = L_A f / 4\pi r_0^2$ to exclude the effect of the adiabatic expansion in the super-radially open flux tubes. While the input Poynting flux ($(L_A f)_0 \propto B_0 f_0 \delta v_0^2$) from the photosphere is different by 4 times each, the differences of the wave energy fluxes in the atmospheres are more than that extent. In particular, the difference is more than one order of magnitude among the three cases, Model Cc−2 β (black dotted), Model (Cc0 β ; green solid), and Model Cc+2 β (red dashed). The sensitive dependence of the wave energy flux in the atmosphere on the input wave energy is because of the suppression of the reflection of the outgoing Alfvén waves as discussed so far.

The middle panel of Figure 7, which compares z_-^2 / z_+^2 , the ratio of the reflected waves to the outgoing waves, exhibits that the wave reflection is suppressed for larger $(L_A f)_0$. One exception is the difference between the second most active case (Cc+2 β ; red dashed) and the most active case (Cc+4 β ; blue dot-dashed). In the upper region, $r - r_0 > 0.01r_0$, the fraction of the reflected component is larger in the most active case, which is opposed to the tendency for the cases with the smaller energy inputs. This is because in the most active case the density decreases faster in the upper region as a result of the smaller (time-averaged) temperature. Then, a finite level of the reflection continues even in the upper region, which also results in the faster decrease of F_A (upper panel of Figure 7).

The bottom panel of Figure 7 compares z_+^2 . This interestingly shows that the wave amplitudes of the outgoing component are comparable in these cases although the energy fluxes are very different. The difference of F_A is mostly owing to the difference of the densities, in addition to the difference of the reflection efficiency.

4.3. Saturation of $L_{K,\text{out}}$ – Enhanced Radiative Loss–

4.3.1. Energetics

We examine the energetics of the stellar winds above the chromosphere by Equation (16). In Figure 8, we show the wind kinetic energy luminosities, $L_{K,\text{out}}$ (filled squares), and the radiation losses, $(L_R f)_{tc}$ (crosses), with the net outgoing Poynting fluxes, $(L_A f)_{tc}$, measured at the top of the chromosphere where $T = 2 \times 10^4 \text{ K}$ of the cases with $B_{r,0}f_0 = 1.25 \text{ G}$. The fraction of the wind kinetic energy,

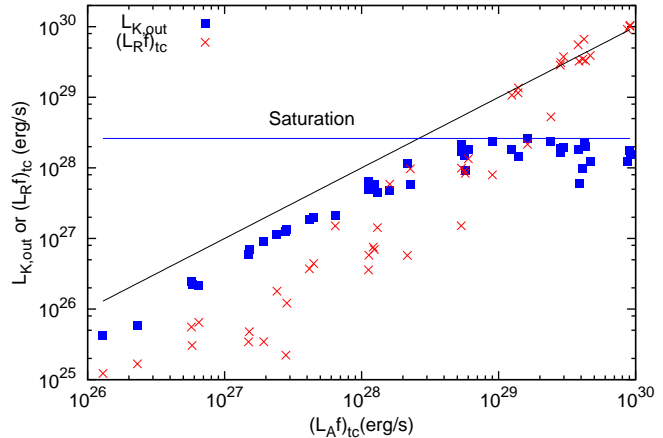


Fig. 8. Kinetic energy, $L_{K,\text{out}}$, (filled squares) and radiation loss, $(L_R f)_{tc}$ (crosses) versus upgoing Poynting flux, $(L_A f)_{tc}$, at the top of the chromosphere of the cases with $B_{r,0}f_0 = 1.25 \text{ G}$. The diagonal line indicates the $x = y$ relation and the horizontal line indicates the saturation level of $L_{K,\text{out}}$.

$L_{K,\text{out}} / (L_A f)_{tc}$, is initially large, with roughly \sim half of $(L_A f)_{tc}$ transferred to the stellar wind. $L_{K,\text{out}}$ increases almost linearly with $(L_A f)_{tc}$, but eventually saturates for large $(L_A f)_{tc}$. Some cases even show considerably smaller $L_{K,\text{out}}$ than other cases with similar $(L_A f)_{tc}$. The saturation of the wind kinetic energy is a consequence of the enhancement of the radiation loss. $(L_R f)_{tc}$ increases with $(L_A f)_{tc}$ much faster than the linear dependence, because the wind density increases as a result of strong driving as we increase the input energy. In the optically thin plasma, the radiation loss is proportional to ρ^2 , and then, $(L_R f)_{tc}$ rapidly increases with $(L_A f)_{tc}$. The fraction of the radiation loss, $(L_R f)_{tc} / (L_A f)_{tc}$, which starts from a much smaller value at small $(L_A f)_{tc}$ than $L_{K,\text{out}} / (L_A f)_{tc}$, is approaching to \approx unity⁵ ($(L_R f)_{tc} = (L_A f)_{tc}$) for large

⁵ In some cases, the radiative losses exceed the injected Poynting fluxes from the top of the chromosphere, $(L_R f)_{tc} / (L_A f)_{tc} > 1$, which seems to break the energy conservation relation. In addition to the Poynting fluxes, however, there are contributions from perturbations of gas pressure (Eq.6) to the energy injections, which we do not take into account in Equation (16). The gas pressure perturbations are due to sound waves nonlinearly generated from Alfvén waves (Kudoh & Shibata 1999; Suzuki & Inutsuka 2006). Although the energy inputs from such sound waves are smaller than the energy inputs from the Alfvén waves,

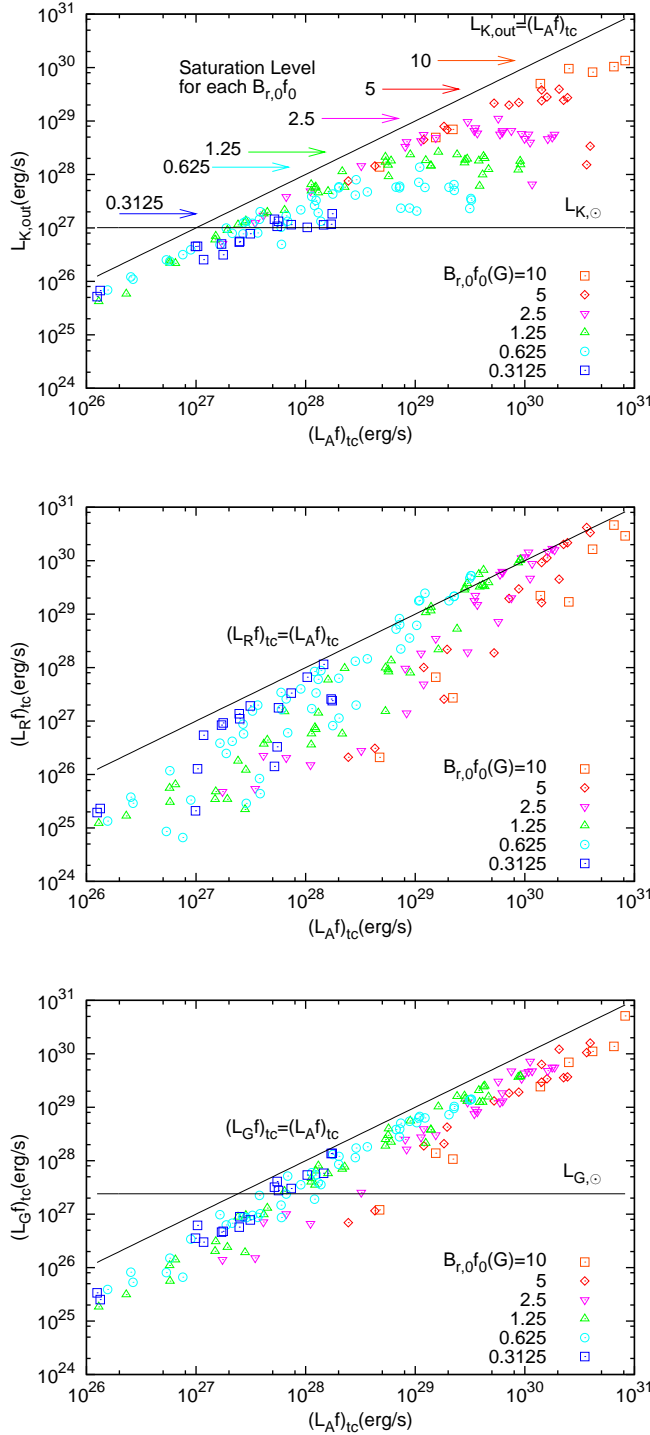


Fig. 9. Energetics of the simulated stellar winds. From top to bottom, kinetic energy, $L_{K,\text{out}}$, radiation loss, $(L_R f)_{\text{tc}}$, and gravitational loss, $(L_G f)_{\text{tc}}$, are shown on outgoing Poynting flux, $(L_A f)_{\text{tc}}$, at the top of the chromosphere. The diagonal line in each panel indicates the $x = y$ relation. In the panels for $L_{K,\text{out}}$ and $(L_G f)_{\text{tc}}$, the present solar level which is estimated by using $\dot{M} = 2 \times 10^{-14} M_{\odot} \text{yr}^{-1}$ and $v_r = 400 \text{ km s}^{-1}$ is also shown by the horizontal lines. In the top panel, the saturation level of $L_{K,\text{out}}$ for each $B_{r,0} f_0$ is indicated by the color arrows.

$(L_A f)_{\text{tc}}$. In this saturated state, the Poynting flux passing through the top of the chromosphere is mostly radiated away in the upper regions. As a result, the fractions transferred to the wind kinetic energies are quite small in these cases, which is observed as the saturation or drop of $L_{K,\text{out}}$ with increasing $(L_A f)_{\text{tc}}$.

Figure 9 displays each term of Equation (16), the kinetic energy luminosity, $L_{K,\text{out}}$ (top panel), the radiation loss, $(L_R f)_{\text{tc}}$ (middle panel), and the gravitational loss, $(L_G f)_{\text{tc}}$ (bottom panel), of the stellar winds with the net outgoing Poynting flux, $(L_A f)_{\text{tc}}$, measured at the top of the chromosphere. Figure 9 clearly shows that the trend –the saturation of $L_{K,\text{out}}$ as a consequence of the enhanced $(L_R f)_{\text{tc}}$ – is universal for the other values of $B_{r,0} f_0$. Furthermore, the saturation level of the kinetic energy luminosity, $L_{K,\text{out,sat}}$, is positively correlated with $B_{r,0} f_0$ as shown in the top panel, where $L_{K,\text{out,sat}}$ is taken from the case which gives the largest $L_{K,\text{out}}$ for each $B_{r,0} f_0$ (Table 3). The nonlinear dissipation of the Alfvén waves can explain the dependence of the saturation level on $B_{r,0} f_0$. Since $B_r = B_{r,0} f_0 r_0^2 / r^2$, $B_{r,0} f_0$ determines the Alfvén speed, v_A , in the wind acceleration region ($1.5r_0 \lesssim r \lesssim 10r_0$). The nonlinearity of Alfvén waves, $\delta v_{\perp} / v_A$, is an important factor which controls the dissipation of Alfvén waves, and larger $\delta v_{\perp} / v_A$ leads to faster dissipation (e.g. Hollweg 1973; Suzuki & Inutsuka 2006). Then, in cases with smaller $B_{r,0} f_0$, the nonlinearity becomes relatively larger because of the smaller v_A in the wind acceleration regions (Suzuki 2012). In these cases, the Alfvén waves dissipate faster at lower altitudes where the densities are higher. As a result, more wave energy is transferred to the radiation losses rather than the wind kinetic energy. On the other hand, in cases with larger $B_{r,0} f_0$ the Alfvén waves can travel to higher altitudes and effectively drive the stellar winds, which gives the higher saturation levels of $L_{K,\text{out}}$. Although our simulations focus on the nonlinear generation of compressive waves as the primary dissipation mechanism of the Alfvén waves, the discussion on the saturation so far can be applied provided that nonlinear dissipation processes, e.g. turbulent cascade, dominantly operate because $\delta v_{\perp} / v_A$ controls the wave dissipation in the same manner. On the other hand, if the dissipation of linear Alfvén waves, e.g. phase mixing due to viscosity and resistivity (Heyvaerts & Priest 1983) or Landau-type damping due to kinetic effects (e.g. Suzuki et al. 2006), was dominant, the saturation would give a different tendency.

We show the wind kinetic energy, $L_{K,\text{out,sat}}$, and the corresponding mass loss rate, \dot{M}_{sat} , of the saturated cases (Table 3) in Figure 10. Both $L_{K,\text{out,sat}}$ and \dot{M}_{sat} are well fitted by power-law functions (solid lines in Figure 10),

$$L_{K,\text{out,sat}} = 2.05 \times 10^{28} \text{ erg s}^{-1} (B_{r,0} f_0)^{1.84}, \quad (21)$$

and

$$\dot{M}_{\text{sat}} = 7.86 \times 10^{-12} M_{\odot} \text{ yr}^{-1} (B_{r,0} f_0)^{1.62}. \quad (22)$$

(See §5.4 for more general expressions with dependences

they are not negligible in active cases.

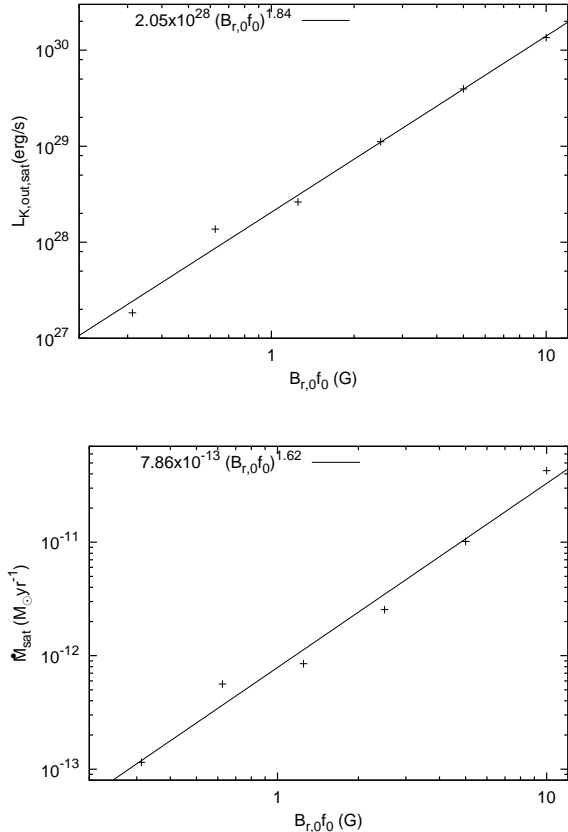


Fig. 10. *Upper panel:* Kinetic energy, $L_{K,\text{out,sat}}$, of the saturated cases for the respective $B_{r,0}f_0$ with $B_{r,0}f_0$. The line is the best fit function, Equation (21). *Lower panel:* Mass loss rate, \dot{M}_{sat} of the saturated cases. The line is the best fit function, Equation (22).

on r_0 and M dependences.) Both relations give the similar dependences on $(B_{r,0}f_0)$.

The comparison between Equations (19) and (21) gives

$$c_E \langle \delta v_0^2 \rangle |_{\text{sat}} \propto (B_{r,0}f_0)^{0.84} \quad (23)$$

for the saturated cases, where we neglect the weak dependence on the photospheric density, ρ_0 . In order to understand this relation, let us start from the dependence of c_E on δv_0^2 in a fixed $(B_{r,0}f_0)$. In the unsaturated state with small $\langle \delta v_0^2 \rangle$, an increase of $\langle \delta v_0^2 \rangle$ enhances c_E , because the reflection of the Alfvén waves is suppressed (§4.2). When one further increases $\langle \delta v_0^2 \rangle$ to the saturated state, c_E starts to decrease on account of the radiation loss as discussed in this section and finally $c_E \langle \delta v_0^2 \rangle$ itself decreases. At the saturation, $c_E \approx 0.05$, which is nearly independent from $(B_{r,0}f_0)$ (Figure 3). Equation (23) indicates that $\langle \delta v_0^2 \rangle$ that gives the saturation of the stellar wind is roughly proportional to $(B_{r,0}f_0)$ (we assume $0.84 \approx 1$). In cases with large $(B_{r,0}f_0)$, large amplitude Alfvén waves can propagate to higher locations owing to larger v_A and accordingly the smaller nonlinearity of the Alfvén waves as discussed so far.

Equations (21) and (22) are the maximum kinetic energy and mass loss rate for given $(B_{r,0}f_0)$. The stan-

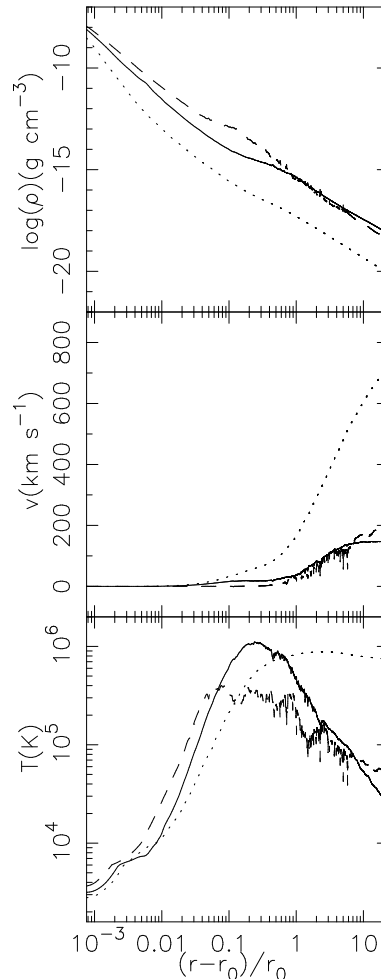


Fig. 11. Comparison of the time-averaged wind structures of three cases tabulated in Table 4. The less active case (Model Dd+3 γ), the intermediate case (Model De+4 γ), and the active case (Model Df+5 γ) are shown in dotted, solid, and dashed lines. From top to bottom, the densities, radial velocities, and temperatures are compared.

dard case for the current solar wind (Model Cb0 α ; Table 2) gives only 8% of the maximum kinetic energy ($L_{K,\text{out}}/L_{K,\text{out,sat}} = 0.08$). Therefore, by increasing δv_0 at the photosphere, the stellar wind kinetic energy could be raised up to 12.5 times but cannot exceed it. In order to get further large kinetic energy, a flux tube with larger $(B_{r,0}f_0)$ is required.

An important point regarding Equations (21) and (22) is that the saturation level is not determined by only $B_{r,0}$ but $B_{r,0}f_0$; open flux tubes need to occupy a sufficient fraction of the stellar surface (*i.e.*, large f_0) in addition to large field strength at the photosphere. This is also consistent with the explanation of the saturated stellar winds from the change of the magnetic topology that closed magnetic loop structure, which is expected to dominantly cover the surface of active stars, inhibits the stellar winds (Wood et al. 2005). A large fraction of closed loops corresponds to a small f_0 , and then, stellar winds arising from such conditions will also become weak in our simulations.

Model	δv_0	$B_{r,0}(\text{kG}) \times f_0$	$h_1 (r_0)$	$(L_{\text{Af}})_0$	$(L_{\text{Af}})_{\text{tc}}$	c_{T}	$\dot{M} (M_{\odot} \text{yr}^{-1})$	$v_{r,\text{out}}$	$L_{\text{K},\text{out}}$	$(L_{\text{Rf}})_{\text{tc}}$
Dd+3 γ	3.79	4/1600	0.1	2.0×10^{30}	1.2×10^{29}	0.061	3.3×10^{-13}	733	5.6×10^{28}	4.9×10^{27}
De+4 γ	5.35	8/3200	0.1	3.9×10^{30}	1.1×10^{30}	0.28	6.0×10^{-12}	145	4.0×10^{28}	4.7×10^{29}
Df+5 γ	7.57	16/6400	0.1	7.8×10^{30}	1.6×10^{30}	0.21	4.0×10^{-12}	191	4.6×10^{28}	1.5×10^{30}

Table 4. Input parameters and outputs for the cases shown in Figure 11. The unit of δv_0 and $v_{r,\text{out}}$ is km s^{-1} , and the unit of L is erg s^{-1} . c_{T} is the surviving fraction of the Alfvén waves from the photosphere to the top of the chromosphere (Equation 15).

4.3.2. Atmospheric Structure

We further study the saturated state of the stellar winds by examining some simulated wind structures. Figure 11 compares the three cases, summarized in Table 4. We select runs with the same $B_{r,0}f_0 = 2.5 \text{ G}$, but different δv_0 . From the first case (Model Dd+3 γ , dotted) through third case (Model Df+5 γ , dashed), the input energy flux ($\propto B_{r,0}f_0\delta v_0^2$) from the photosphere increases by twice each.

From the first case (Model Dd+3 γ , dotted) to the second case (Model De+4 γ , solid), the atmospheric structure drastically changes. The density of the second case is ~ 10 times larger in the chromosphere and corona and ~ 100 times larger in the stellar wind region. On the contrary, the wind speed becomes very slow because the dense wind cannot be effectively accelerated. As a result of the high density, the radiative loss ($(L_{\text{Rf}})_{\text{tc}}$ in Table. 4) of the second case is nearly 100 times larger than that of the first case, even though the input wave energy is only twice. Although the mass loss rate ($\dot{M} \propto \rho v_r$ in Table. 4) is also larger due to the enhanced density, the kinetic energy luminosity ($L_{\text{K},\text{out}} \propto \rho v_r^3$ in Table. 4) slightly decreases because of the low velocity, which is recognized as the saturation of $L_{\text{K},\text{out}}$ in the top panel of Figure 9. While the maximum temperature of the second case is higher than that of the first case, the temperature decreases more rapidly because the thermal conduction is relatively ineffective against the adiabatic cooling in the denser corona.

The comparison between the second (Model De+4 γ) and third (Model Df+5 γ) cases exhibits an example of a saturated state. The overall density and velocity structures are quite similar. Then, both \dot{M} and $L_{\text{K},\text{out}}$ from these two cases are similar; the mass loss rate also saturates at this stage. By a close look one can see that the third case gives slightly larger density from the chromosphere to the low coronal region, which leads to the ~ 3 times larger radiative loss as shown in Table. 4. The maximum temperature of the third case is smaller than that of the second case because of the enhanced radiative loss.

5. Discussions

5.1. Comparison with Wood et al.

In this section, we compare our results with the results by Wood et al. (2002; 2005). They derived the mass loss rates by comparing the observed Ly α absorptions of nearby G, M, K-type stars with the hydrodynamical simulations on the assumption of the spherical symmetry and the steady-state with a fixed terminal speed ($=400 \text{ km s}^{-1}$) of the stellar winds. Although the derived mass loss rates might have uncertainties because of these assump-

tions, this work is the best effort to observationally determine the mass loss rates of the low-mass stars.

5.1.1. Evolution with X-ray flux

As a key presentation in their papers, they plotted the mass loss rates with the X-ray fluxes of the observed solar-type stars; we here put our results in the same diagram. The mass loss rates obtained in our simulations can be directly compared with the results by Wood et al.(2002; 2005). On the other hand, the X-ray fluxes of our simulations considerably underestimate the actual X-ray fluxes because our simulations only treat open flux tubes although it is expected that the observed X-rays are mainly from closed loops. From an observational point of view, the UV flux from solar-type stars is well-correlated with the X-ray flux (Ayres 1997). Based on these considerations, we use the radiation flux from the gas with $T > 2 \times 10^4 \text{ K}$.

In order to compare our results with the observed X-ray fluxes, F_{X} , we need to estimate a conversion factor, c_r , from the radiation flux from the gas with $T \geq 2 \times 10^4 \text{ K}$ in the simulated open flux tubes to the actual X-ray flux averaged over the entire stellar surface, where c_r is explicitly in an equation,

$$F_{\text{X}} = c_r \frac{(L_{\text{Rf}})_{\text{tc}}}{4\pi r_0^2}. \quad (24)$$

Here, $\frac{(L_{\text{Rf}})_{\text{tc}}}{4\pi r_0^2}$ is the radiation flux from the gas with $T \geq 2 \times 10^4 \text{ K}$ in the open flux tubes. While it does not include the X-ray from closed loops as discussed above, it includes the radiation in the UV range in addition to the X-ray; c_r could be either larger or smaller than unity. Because we do not have a quantitatively accurate way to estimate c_r , we simply choose a value of c_r to give a reasonable fit to the observation. In Figure 12, we show our results with $c_r = 2$ in comparison with the observed data. From top to bottom, we compare the mass loss rates, \dot{M} , ram pressures, $\dot{M}v_{r,\text{out}}$, and kinetic energy luminosities, $\dot{M} \frac{v_{r,\text{out}}^2}{2}$, divided by the surface areas of the stars and normalized by the current solar level. The three panels essentially compare $\rho v_{r,\text{out}}$, $\rho v_{r,\text{out}}^2$, and $\rho v_{r,\text{out}}^3$. We use $\dot{M}_{\odot} = 2 \times 10^{-14} M_{\odot} \text{ yr}^{-1}$ and $v_{\odot} = 400 \text{ km s}^{-1}$ as the normalizations in Figure 12 according to Wood et al. (2002; 2005). Since they assume the same wind speed $= 400 \text{ km s}^{-1}$ for the different stars, we put the observed data points at the same relative positions in the three panels.

One can recognize that our simulations exhibit more clear saturations in $\rho v_{r,\text{out}}^2$ and $\rho v_{r,\text{out}}^3$. On the other hand, $\rho v_{r,\text{out}}$ shows an increasing trend rather than a saturation. This is mainly because active cases with large radiation fluxes give systematically slower wind velocities

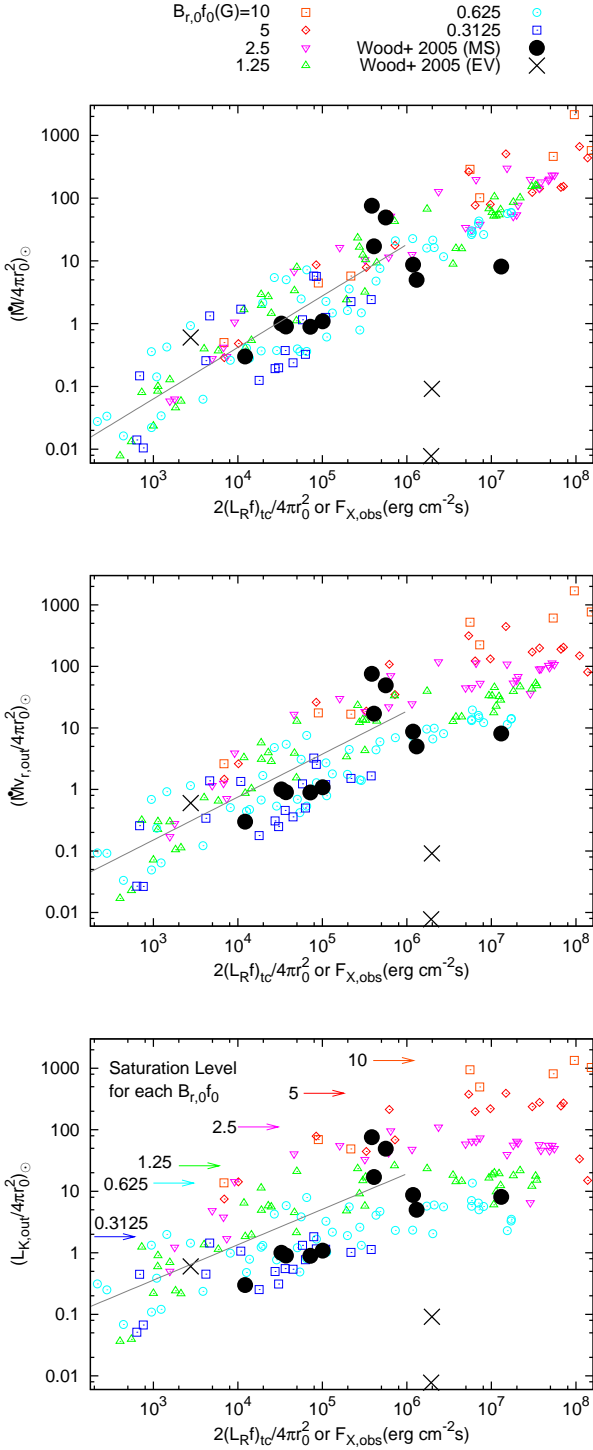


Fig. 12. Comparison of the simulation results (color symbols) with the observed data by Wood et al. (2002; 2005; big black symbols; circles indicate main sequence stars and crosses are evolved stars.) The horizontal axis displays the X-ray flux (for Wood et al. data) or the radiation from open flux tube regions with $T \geq 2 \times 10^4$ K multiplied by $c_r = 2$ (for our results; see *text* for detail). From top to bottom we compare the mass loss rates ($\propto \rho v_{r,\text{out}}$), the ram pressures ($\propto \rho v_{r,\text{out}}^2$), and the kinetic energy luminosities ($\propto \rho v_{r,\text{out}}^3$) divided by the stellar surface areas and normalized by the present-day solar level ($\dot{M} = 2 \times 10^{-14} M_\odot \text{yr}^{-1}$ and $v = 400 \text{ km s}^{-1}$). Then, the observational data points are plotted at the same relative positions in the three panels, because Wood et al. (2002; 2005) adopt the constant $v = 400 \text{ km s}^{-1}$ for their hydrodynamical simulations to estimate the observational \dot{M} . The solid line in each panel is the power-law fit to the simulation data with $F_X < 10^6 \text{ erg cm}^{-2} \text{ s}^{-1}$ shown in Equation (25).

(Fig. 5). The Ly α absorptions in the hydrogen walls of astrospheres are correlated with the ram pressures of stellar winds (Wood & Linsky 1998). In this sense, the ram pressure (the middle panel) is a more physically plausible variable. In this panel the simulation results explains the observed distribution quite well except for the evolved stars.

Wood et al. (2005) obtained $\dot{M} \propto F_X^{1.34 \pm 0.18}$ from their data of the “unsaturated” stars. On the other hand, a theoretical model by Holzwarth & Jardine (2007) gives a shallower dependence, $\dot{M} \propto F_X^{0.5}$. We perform power-law fits to our simulation data with $F_X \leq 10^6 \text{ erg cm}^{-2} \text{ s}^{-1}$ corresponding to the unsaturated cases for the three panels of Figure 12:

$$\begin{aligned} \frac{\dot{M}}{4\pi r_0^2} &= \frac{\dot{M}_\odot}{4\pi R_\odot^2} \left(\frac{F_X}{2.9 \times 10^4 \text{ erg cm}^{-2} \text{ s}^{-1}} \right)^{0.82} \\ \frac{\dot{M}}{4\pi r_0^2} v_{\text{out}} &= \frac{\dot{M}_\odot}{4\pi R_\odot^2} v_\odot \left(\frac{F_X}{1.5 \times 10^4 \text{ erg cm}^{-2} \text{ s}^{-1}} \right)^{0.70} \\ &= \frac{\dot{M}_\odot}{4\pi R_\odot^2} v_{630} \left(\frac{F_X}{2.9 \times 10^4 \text{ erg cm}^{-2} \text{ s}^{-1}} \right)^{0.70} \quad (25) \\ \frac{\dot{M}}{4\pi r_0^2} v_{\text{out}}^2 &= \frac{\dot{M}_\odot}{4\pi R_\odot^2} v_\odot^2 \left(\frac{F_X}{5.9 \times 10^3 \text{ erg cm}^{-2} \text{ s}^{-1}} \right)^{0.58} \\ &= \frac{\dot{M}_\odot}{4\pi R_\odot^2} v_{630}^2 \left(\frac{F_X}{2.9 \times 10^4 \text{ erg cm}^{-2} \text{ s}^{-1}} \right)^{0.58}, \end{aligned}$$

where again the normalizations are $\dot{M}_\odot = 2 \times 10^{-14} M_\odot \text{yr}^{-1}$ and $v_\odot = 400 \text{ km s}^{-1}$. Most of the unsaturated cases with smaller inputs $(L_{\text{A}f})_0$ of our simulations give faster wind speeds than v_\odot . Then, we are also showing the relations of $\dot{M} v_{\text{out}}$ and $\dot{M} v_{\text{out}}^2$ with the normalization of $v_{630} = 630 \text{ km s}^{-1}$ for the wind speeds instead of v_\odot , which gives the exactly same normalization of $F_X = 2.9 \times 10^4 \text{ erg cm}^{-2} \text{ s}^{-1}$ as that for \dot{M} . The value for the velocity normalization is interestingly close to the escape velocity, $v_{\text{esc},0} = 618 \text{ km s}^{-1}$. The above scaling relations show that as multiplied by v_{out} once and twice, the power-law index decreases. This is because the stellar wind becomes slower as the wind density ($\sim \rho_{\text{tc}}$) increases with increasing $(L_{\text{A}f})_0$ (§4.1). Interestingly enough, the obtained power-law index falls between the values by Wood et al. (2005) and by Holzwarth & Jardine (2007).

The top panel as well as the middle and bottom panels of Figure 12 further show horizontal scatters of the simulation data that exceed one order of magnitude. This indicates that the X-ray fluxes could vary even though the mass loss rates are unchanged, which actually occur during the 11-year cycle of the sun.

5.1.2. Time Evolution –Speculative Scenario–

In realistic situations, the average $Br_0 f_0$ of the open flux tubes of a sun-like star would change with time. Comparison of the observed values with the simulation results in the middle or bottom panels of Figure 12 enables us to raise a following speculative scenario on the time evolution of the stellar wind (Figure 13). In Figure 12 stars generally evolve from the right (larger F_X) to the left

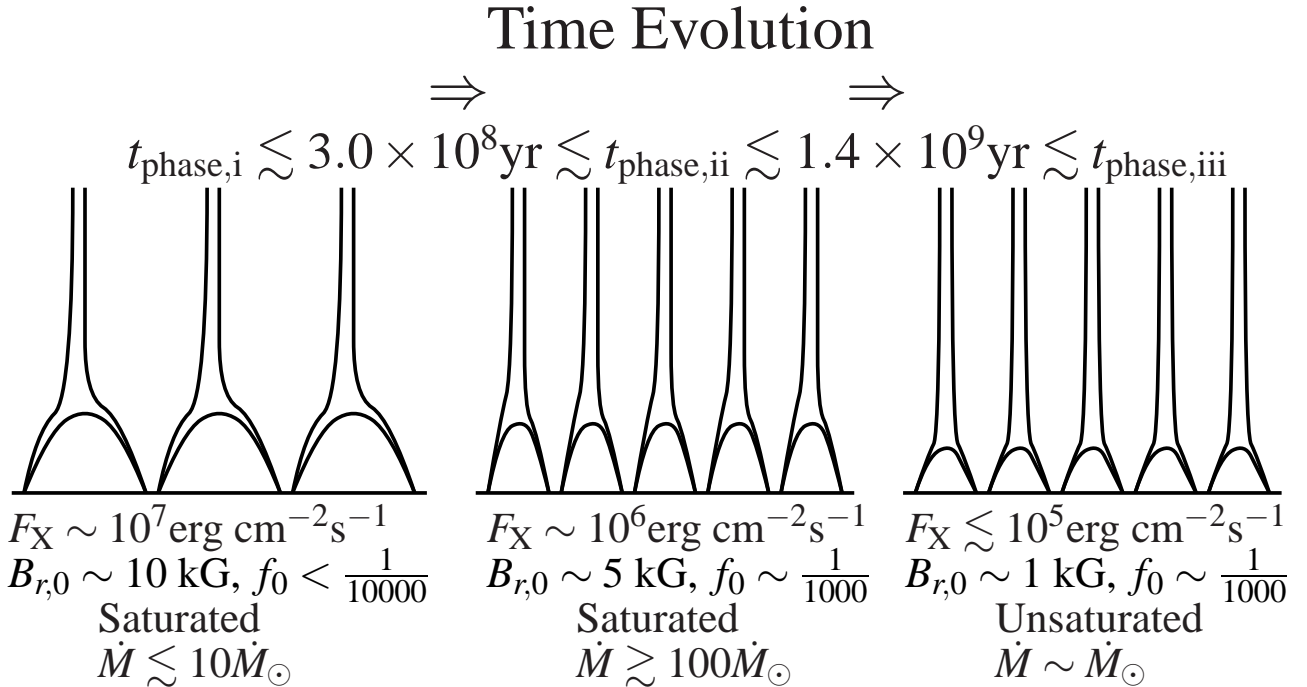


Fig. 13. Speculative scenario of the time evolution of properties of open flux tubes based on Wood et al. (2002; 2005). (see §5.1.2 for details.)

(smaller F_X). The most active star among the observed data at $F_X = 1.3 \times 10^7 \text{ erg cm}^{-2} \text{ s}^{-1}$ is well explained by a small value of $B_{r,0} f_0 < 1 \text{ G}$. Probably, this star is mostly covered by closed loops and the filling factor of open flux tubes is very small, say $f_0 \lesssim 1/10000$. Then, even if the photospheric field strength is strong, e.g. $B_{r,0} \sim 10 \text{ kG}$, $B_{r,0} f_0$ becomes small $< 1 \text{ G}$, which gives the low saturation level of the stellar wind. With the stellar evolution, the magnetic topology is relaxed so that f_0 increases to $\sim 1/1000$. At this stage with $F_X \sim 10^6 \text{ erg cm}^{-2} \text{ s}^{-1}$, the stellar wind flux increases owing to the increase of f_0 , although stars are still in the saturated state. In the subsequent evolution, $B_{r,0}$ decreases with time and stars are deviated from the saturated state. The stellar wind kinetic energies eventually settle down to the current solar level.

We should be very careful when comparing the evolution of magnetic fields in this scenario with observed magnetic fields in young active stars (e.g. Saar 2001; Donati & Landstreet 2009), because observationally determined $B_{r,0}$ and f_0 sensitively depend on the spatial resolution. Even on the sun, kilo-Gauss patches in coronal holes are a recent new discovery by the high resolution observation by SOT/HINODE (Tsuneta et al. 2008). Observations with lower resolutions would give smaller $B_{r,0}$ as a result of spatial smoothing, and accordingly the derived f_0 would be larger, because $B_{r,0} f_0$ is independent from the spatial resolution. As discussed previously, the contribution from close magnetic loops, of which the strength also depends on the spatial resolution, needs to be taken into account.

In this scenario, an increase of f_0 , namely the change of the magnetic topology, plays an important role in the

evolution of the mass loss from sun-like stars. In this context, it is similar to the consideration raised by Wood et al. (2005) in which closed magnetic structures that cover the surface of very active stars inhibit the stellar winds but gradual opening of these closed fields liberate the stellar winds streaming out. In our scenario, however, the radiation loss which is enhanced by the increase of the density in the atmospheres is as important in the saturation of the stellar winds as the change of the magnetic topology.

We can infer the time evolution in a little more quantitative way by using F_X as a tracer of stellar ages. X-ray observations of sun-like stars give a negative correlation between X-ray luminosity, L_X , and stellar age, t_{age} , (Maggio et al. 1987), with some of them are indirectly connected through stellar rotation periods (Güdel et al. 1997). Güdel (2007) derived a relation,

$$L_X \approx (3 \pm 1) \times 10^{28} \left(\frac{t}{10^9 \text{ yr}} \right)^{-1.5 \pm 0.3} \text{ erg s}^{-1}, \quad (26)$$

for sun-like stars. Following the speculated scenario in Figure 13, we classify the evolution into the three phases in terms of $L_X = 4\pi r_0^2 F_X$ estimated from our simulations:

- (i): saturated & weak wind phase:
 $F_X \gtrsim 3.0 \times 10^6 \text{ erg cm}^{-2} \text{ s}^{-1}$ or $L_X \gtrsim 1.8 \times 10^{29} \text{ erg s}^{-1}$
 $t_{\text{phase,i}} \lesssim 3.0 \times 10^8 \text{ yr}$
- (ii): saturated & strong wind phase:
 $3.0 \times 10^5 \text{ erg cm}^{-2} \text{ s}^{-1} \lesssim F_X \lesssim 3.0 \times 10^6 \text{ erg cm}^{-2} \text{ s}^{-1}$
or $1.8 \times 10^{28} \text{ erg s}^{-1} \lesssim L_X \lesssim 2 \times 10^{29} \text{ erg s}^{-1}$
 $3.0 \times 10^8 \text{ yr} \lesssim t_{\text{phase,ii}} \lesssim 1.4 \times 10^9 \text{ yr}$
- (iii): unsaturated wind phase:

$$F_X \lesssim 3.0 \times 10^5 \text{ erg cm}^{-2}\text{s}^{-1} \text{ or } L_X \lesssim 1.8 \times 10^{28} \text{ erg s}^{-1}$$

$$t_{\text{phase,iii}} \gtrsim 1.4 \times 10^9 \text{ yr}$$

Here, the timescale of each phase is estimated by using Equation (26).

Combining Equations (25) and (26), we can further derive the scalings for the stellar winds as a function of time for the unsaturated cases of our simulations:

$$\frac{\dot{M}}{4\pi r_0^2} = 1.6 \times \frac{\dot{M}_\odot}{4\pi R_\odot^2} \left(\frac{t}{t_\odot}\right)^{-1.23},$$

$$\frac{\dot{M}}{4\pi r_0^2} v_{\text{out}} = 1.5 \times \frac{\dot{M}_\odot}{4\pi R_\odot^2} v_{630} \left(\frac{t}{t_\odot}\right)^{-1.05}, \quad (27)$$

$$\frac{\dot{M}}{4\pi r_0^2} v_{\text{out}}^2 = 1.4 \times \frac{\dot{M}_\odot}{4\pi R_\odot^2} v_{630}^2 \left(\frac{t}{t_\odot}\right)^{-0.87},$$

where $t_\odot = 4.6 \times 10^9$ yr. These time dependences are less steep than the relation obtained in Wood et al. (2005), $\dot{M} \propto t^{-2.33 \pm 0.55}$. This is mainly because our derived relation of \dot{M} on F_X (Equation 25) is shallower than the relation obtained in Wood et al. (2005), $\dot{M} \propto F_X^{1.34 \pm 0.18}$. Also, Wood et al. (2005) adopted a different relation of $F_X \propto t^{-1.74 \pm 0.34}$ (Ayres 1997) from the relation we are using (Equation 26), which further contributes to the shallower dependence of Equation (27).

5.2. Faint Young Sun Paradox

The luminosity of sun-like stars gradually increases during the main sequence phase. Based on the standard stellar evolution calculation, the luminosity of the sun is 20-30% smaller at early times (Gough 1981). As a result, the surface temperature on the earth is expected to be below the freezing temperature before ~ 2 billion years ago. On the other hand, liquid water already existed at that time on the earth as well as on the mars (Sagan & Mullen 1972; Karhu & Epstein 1986; Feulner 2011), which looks contradictory, known as the ‘faint young Sun paradox’. A high level of green house effects (Owen et al. 1979; Kasting 1997), and modification of the solar model (Whitmire et al. 1995; Minton & Malhotra 2007) are the two major possibilities which can solve the problem. We here discuss effects of the strong mass loss of the Sun (Willson et al. 1987; Sackmann & Boothroyd 2003).

As already discussed in §4.2.2, the saturation level of the stellar winds is determined by $B_{r,0} f_0$. The top panel of Figure 9 and Figure 12 indicate that stars with large $B_{r,0} f_0$ ($\sim 5\text{-}10\text{G}$) could drive $\sim 500 - 1000$ times stronger mass loss with the X-ray flux in the observed range ($F_X \leq 2 \times 10^7 \text{ erg cm}^{-2}\text{s}^{-1}$), although such a large mass loss rate has not been observed so far. If such a strong mass loss actually continues ~ 1 billion years as discussed in §5.1.2 and Figure 13, it contributes to the decrease of stellar masses.

1000 times of \dot{M} during 1 billion years gives the mass loss of $0.02M_\odot$. If this is true in the Sun, the initial mass is 2 % larger than the present Sun. An increase of the stellar mass influences the radiation flux on planets around a star in two ways. First, the stellar radiation itself is

larger; in sun-like stars, the luminosity, L , can be scaled by $L \propto M^{4.75}$ (Kippenhahn & Weigert 1990; Whitmire et al. 1995). A 2% larger M gives ≈ 10 % larger L . Second, the orbital radius, a_p , of a planet shrinks in a manner to keep Ma_p constant (Whitmire et al. 1995; Minton & Malhotra 2007). Then, the radiation flux ($\propto 1/a_p^2$) on the planet increases by ≈ 4 %. As the sum of these two effects, the radiation flux increases ≈ 15 %, which could considerably compensate the early faint sun and avoid the freezing temperature on the earth.

In this paper, we are focusing on the quasi-steady component of the stellar winds from open flux tubes during the main sequence phase. In active sun-like stars, coronal mass ejections (CMEs), which probably involves magnetic reconnections of closed loops (e.g. Ohya & Shibata), might significantly contribute to the mass losses. Aarnio et al. (2012) estimated mass loss rates by CMEs from pre-main sequence stars by extrapolating the observed relation between X-ray flare energy and CME mass in the present Sun. Although their main target is not CMEs during early main sequence phases, which is crucial in the faint young Sun paradox, we can infer by a simple interpolation that the relative contribution of CMEs to the total mass loss is larger at earlier times than the present contribution ($\sim 10\%$).

5.3. Extended Variable Chromosphere

We have discussed in §4.2 that, when increasing the input wave energy from the current solar level, the chromospheric materials are lifted by the magnetic pressure of the Alfvén waves (§4.2.2 and Figure 6). An extended chromosphere is a universal feature in our simulations with relatively large energy inputs. Another important aspect is that the atmospheres behave more dynamically. In particular, the transition regions move up and down because of the thermally unstable region ($T \gtrsim 10^5$ K) of the radiative cooling function (Landini & Monsignori-Fossi 1990; Sutherland & Dopita 1993). Figure 14 shows snapshot structures (solid and dashed lines) of an active case (Model Dd+4 γ) with $\delta v_0 = 5.35 \text{ km s}^{-1}$, $B_{r,0} = 4 \text{ kG}$, $f_0 = 1/1600$, and $h_1 = 0.1r_0$, in comparison with the time-averaged wind structure (dotted lines). In the time-averaged structure the temperature gradually increases from $T = 10^4$ K at $r \approx 0.01r_0$ to $T = 10^6$ K at $r \approx 0.15r_0$. However, one can recognize from the snapshots that this is simply a result of the long-time average. The snapshot structures at the two different times show that the sharp transition region moves up and down; at $t = 258.2$ hr (solid lines) the chromosphere is extended up to $r \approx 0.2r_0$, while at $t = 269.6$ hr (dashed lines) the corona is getting down to $r \approx 0.01r_0$ with a part of dense coronal gas falling down (Pinto et al. 2009).

Figure 15 displays the time evolution of the top of the chromosphere (=the base of the transition region), r_{tc} , at $T = 2 \times 10^4$ K, of Model Dd+4 γ . The figure clearly shows that the transition region moves up and down dynamically. Within the displayed duration of 72 hours (=3 days), the chromosphere extends to $\gtrsim 1.1r_0$ by 3 times. On the other hand, its motion is sometimes quite fast

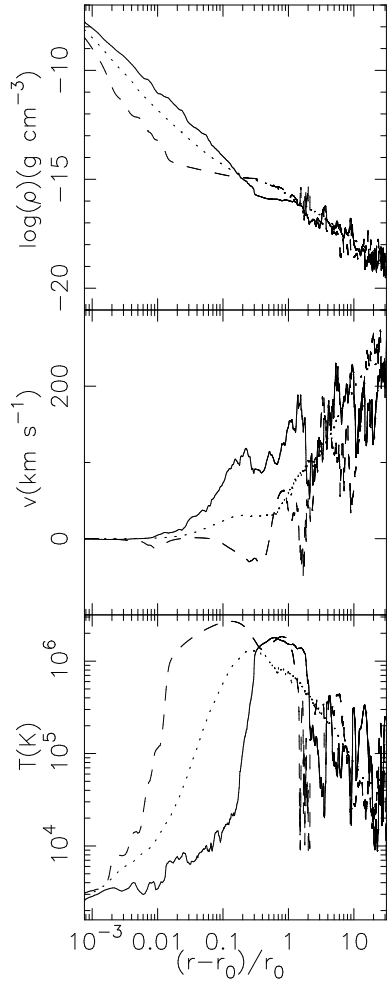


Fig. 14. Comparison of snap-shot wind structures at $t = 258.2$ hr (solid) and $t = 269.6$ hr (dashed) for Model Dd+4 γ . The dotted lines are the time-average between $t = 92.45$ hr and 369.7 hr.

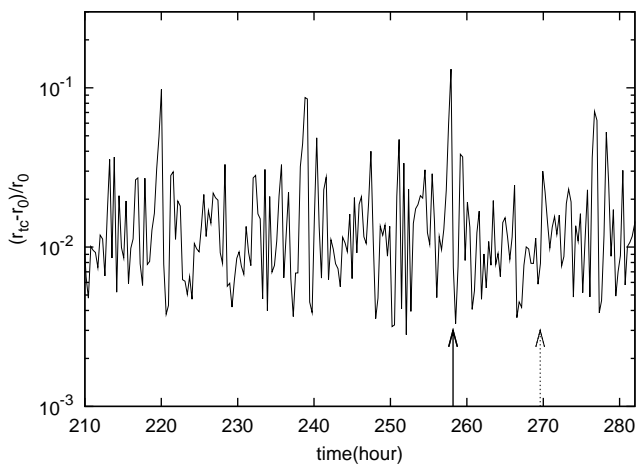


Fig. 15. Time evolution of the top of the chromosphere, r_{tc} , of Model Dd+4 γ . The times at which the snap-shot structures are displayed in Figure 14 are indicated by the arrows.

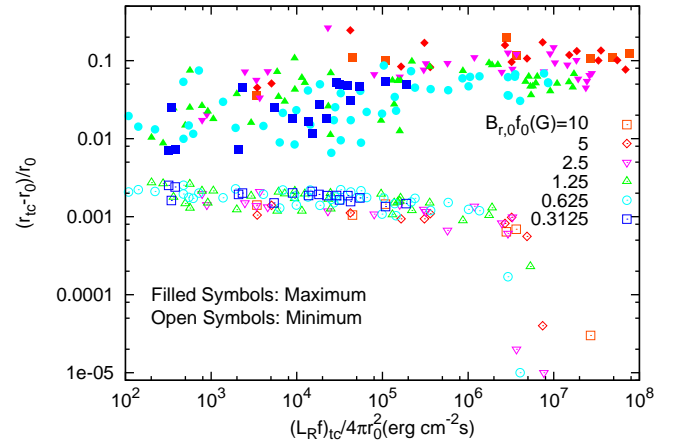


Fig. 16. Location of the top of the chromosphere, r_{tc} , on radiation flux of each run. The filled symbols distributed in the upper half of the panel indicate the maximum heights during the simulations, and the open symbols near the bottom of the panel indicate the minimum heights. In some cases with large radiation flux, $(L_{Rf})_{tc}/4\pi r_0^2$, the minimum of r_{tc} is below the displayed region in the panel.

with the timescale less than an hour; for instance, from $t = 250$ hr to 253 hr, the transition region moves from $1.003r_0$ to $1.05r_0$ with the timescale of 10 minutes. We checked the Fourier transformation of the time-sequence data in Figure 15 to find a roughly flat spectrum without any distinct features (not shown). This indicates that the motion of the transition region does not show clear characteristic timescales but is stochastic with the timescale from minutes to a day. This is because the timescale is controlled by the multiple processes of the wave heating, the radiative cooling, and the thermal conduction. The timescale of the wave heating is an order of minutes, which corresponds to the periods of the injecting perturbations from the photosphere. On the other hand, the timescale of the radiative cooling and the thermal conduction could be large depending on the background physical condition (Shibata & Yokoyama 2002). For instance, the timescale, τ_c , of the thermal conduction can be estimated (Shibata & Yokoyama 2002) as

$$\tau_c \approx 3 \left(\frac{\rho_{tr}}{10^{-15} \text{ g cm}^{-3}} \right) \left(\frac{\Delta r_{tr}}{0.1 r_0} \right)^2 \left(\frac{T}{10^6 \text{ K}} \right)^{-5/2} \text{ hr}, \quad (28)$$

where ρ_{tr} is the density at the transition region and Δr_{tr} is the width of the transition region. The equation shows that τ_c sensitively depends on Δr_{tr} . For the typical condition of the present-day sun, $\Delta r_{tr} < 0.01r_0$, which gives $\tau_c < 20$ min. In active stars, e.g. Model Dd+4 γ in Figure 14, Δr_{tr} could be large enough to give $\tau_c \sim$ hours – a day.

Recently, Czesla et al. (2012) observed the atmosphere of a planet-hosting young star, CoRoT-2a, by using the technic of the Rossiter-McLaughlin effect. They reported that it could have a very thick chromosphere with height of 10-20% of the radius, which is much larger than the

chromosphere of the present Sun which is only up to < 1% of the radius. Moreover, they observed an asymmetry in the chromospheric Rossiter-McLaughlin effect, which might arise from inhomogeneities of the chromospheric structure.

Figure 16 shows the height of the chromosphere of each simulation run. In the figure, we plot both the maximum (filled symbols) and minimum (open symbols) values of r_{tc} at $T = 2 \times 10^4$ K during the time evolution of each simulation. In cases with small radiation flux, the differences between the maximum and minimum heights are small and r_{tc} is typically $0.01r_0$, which is consistent with the present-day Sun (e.g. Imada et al.2011). As the radiation flux increases, the maximum height increases and the minimum height decreases, namely in active cases the transition regions largely move up and down. The minimum heights in cases with relatively large radiation flux (in the right part of the figure) are considerably small, $r_{tc} - r_0 < 10^{-4}r_0 (= 70 \text{ km})$. Moreover in some cases the minimum heights are in the outside of the displayed range. In these cases, the temperature increases to $T > 2 \times 10^4$ K from the next mesh ($\approx 10^{-5}r_0 = 7 \text{ km}$) to the photosphere at some instants.

5.4. General Scalings of $L_{K,\text{out}}$ & \dot{M}

In our simulations, we consider the star with the same stellar parameters as the sun, $M = M_\odot$, $r_0 = R_\odot$, $T_{\text{eff}} = 5780 \text{ K}$, and $\rho_0 = 10^{-7} \text{ g cm}^{-3}$. Then, the scaling relations for $L_{K,\text{out}}$ and \dot{M} in Equations (19) and (20) have been derived for the fixed stellar parameters. Leaving the basic stellar parameters as variables, we can derive more general expressions for $L_{K,\text{out}}$ and \dot{M} :

$$\begin{aligned} L_{K,\text{out}} &= c_E(L_A f)_0 = c_E \Phi_B \sqrt{\frac{\rho_0}{4\pi}} \langle \delta v_0^2 \rangle \\ &= 2.1 \times 10^{27} \text{ erg s}^{-1} \left(\frac{c_E}{0.017} \right) \left(\frac{r_0}{R_\odot} \right)^2 \left(\frac{\rho_0}{10^{-7} \text{ g cm}^{-3}} \right)^{1/2} \\ &\quad \left(\frac{B_{r,0} f_0}{1.25 \text{ G}} \right) \left\langle \left(\frac{\delta v_0}{1.34 \text{ km s}^{-1}} \right)^2 \right\rangle, \end{aligned} \quad (29)$$

and

$$\begin{aligned} \dot{M} &= c_M \frac{(L_A f)_0 r_0}{GM} = c_M \Phi_B \sqrt{\frac{\rho_0}{4\pi}} \frac{\langle \delta v_0^2 \rangle r_0}{GM}, \\ &= 2.2 \times 10^{-14} M_\odot \text{ yr}^{-1} \left(\frac{c_M}{0.023} \right) \left(\frac{r_0}{R_\odot} \right)^3 \left(\frac{M}{M_\odot} \right)^{-1} \\ &\quad \left(\frac{\rho_0}{10^{-7} \text{ g cm}^{-3}} \right)^{1/2} \left(\frac{B_{r,0} f_0}{1.25 \text{ G}} \right) \left\langle \left(\frac{\delta v_0}{1.34 \text{ km s}^{-1}} \right)^2 \right\rangle \quad (30) \end{aligned}$$

where the relation for \dot{M} is derived in a similar manner to the Reimers (1975) formula (see also Schröder & Cuntz 2005).

These relations should be tested by numerical simulations with stars with different masses, radii, and photospheric densities, which is our future work. It should be noted that the variables in Equations (29) and (30) are not independent each other. For example, limiting to low-mass ($M \lesssim M_\odot$) main sequence stars, r_0 is related to M ,

$r_0 \propto M^{0.8}$ (§22 of Kippenhahn & Weigert 1990). Also, the density, ρ_0 , at a photosphere can be estimated from the stellar basic parameters. For instance, in the cool star condition with effective temperature, $4000 \text{ K} \lesssim T_{\text{eff}} \lesssim 6000 \text{ K}$, $\rho_0 \propto \left(\frac{M}{r_0^2} \right)^{0.6} T_{\text{eff}}^{-3}$ (§9 of Gray 1992; Suzuki 2007). Using these dependences and $T_{\text{eff}} \propto M^{0.4}$ (§22 of Kippenhahn & Weigert 1990), we can replace the dependences on r_0 and ρ_0 in Equations (29) and (30) with the dependences on M :

$$\begin{aligned} L_{K,\text{out}} &= 2.1 \times 10^{27} \text{ erg s}^{-1} \left(\frac{c_E}{0.017} \right) \left(\frac{M}{M_\odot} \right)^{0.82} \\ &\quad \left(\frac{B_{r,0} f_0}{1.25 \text{ G}} \right) \left\langle \left(\frac{\delta v_0}{1.34 \text{ km s}^{-1}} \right)^2 \right\rangle, \end{aligned} \quad (31)$$

and

$$\begin{aligned} \dot{M} &= 2.2 \times 10^{-14} M_\odot \text{ yr}^{-1} \left(\frac{c_M}{0.023} \right) \left(\frac{M}{M_\odot} \right)^{0.62} \\ &\quad \left(\frac{B_{r,0} f_0}{1.25 \text{ G}} \right) \left\langle \left(\frac{\delta v_0}{1.34 \text{ km s}^{-1}} \right)^2 \right\rangle, \end{aligned} \quad (32)$$

Equation (30) or (32) could be a general formula to estimate mass loss rates of stars with a surface convection zone (see also Cranmer & Saar 2011). Once the basic stellar parameters, r_0 , M , and T_{eff} , are obtained, Equation (30) or (32) has the three undetermined parameters, c_M , $(B_{r,0} f_0)$, and δv_0 . One can use a typical value, $c_M \approx 0.02$ from the simulation results. δv_0 is expected to be a fraction of the sound speed at the surface; $\delta v_0 = 1.34 \text{ km s}^{-1}$ of the standard case corresponds to $\sim 20\%$ of the sound speed. $(B_{r,0} f_0)$, magnetic field strength in *open field regions*, is the most unknown parameter among the three. If \dot{M} is obtained by other methods, Equation (30) or (32) can be used to derive $B_{r,0} f_0$ in the opposite way.

We also show general formulae for the saturated values, Equations (21) and (22), with taking into account the dependences on M and r_0 :

$$\begin{aligned} L_{K,\text{out,sat}} &= 2.05 \times 10^{28} \text{ erg s}^{-1} (B_{r,0} f_0)^{1.84} \left(\frac{r_0}{R_\odot} \right)^2, \\ &= 2.05 \times 10^{28} \text{ erg s}^{-1} (B_{r,0} f_0)^{1.84} \left(\frac{M}{M_\odot} \right)^{1.6} \quad (33) \end{aligned}$$

and

$$\begin{aligned} \dot{M}_{\text{sat}} &= 7.86 \times 10^{-12} M_\odot \text{ yr}^{-1} (B_{r,0} f_0)^{1.62} \left(\frac{r_0}{R_\odot} \right)^3 \left(\frac{M}{M_\odot} \right)^{-1}, \\ &= 7.86 \times 10^{-12} M_\odot \text{ yr}^{-1} (B_{r,0} f_0)^{1.62} \left(\frac{M}{M_\odot} \right)^{1.4}, \end{aligned} \quad (34)$$

where we here again use $r_0 \propto M^{0.8}$ for low-mass main sequence stars.

5.5. Stellar Rotation

It is expected that stellar rotation is an important ingredient in determining stellar magnetic activities (Skumanich 1972; Ayres 1997; Güdel et al. 1997; Linsky

et al. 2012). Probably related the steep differential rotation owing to the fast rotation of young active stars (Hotta & Yokoyama 2011), the magnetic field is effectively amplified in fast rotating solar-type stars (Gondoin 2012). We take into account the effects of the strong magnetic fields on the stellar winds by incorporating the wide ranges of the parameters on the magnetic field.

In addition to the generated magnetic field strength, the stellar rotation directly affects the dynamics of stellar winds through the magnetocentrifugal force (Weber & Davis 1967; Cohen et al. 2010). The angular momentum of a star is outwardly transported by the magnetorotating wind, which is the main cause of the deceleration of the stellar rotation (Matt et al. 2012). We do not take into account this effect in our simulations. We here briefly discuss possible roles of the magnetocentrifugal force in the dynamics of the stellar winds.

In general, stronger magnetic field and faster rotation affects the dynamics of stellar winds. Magnetic energy per mass in magnetorotating winds (Weber & Davis 1967; see also §9 of Lamers & Cassinelli 1999) is written as

$$\epsilon_B = -\frac{r\Omega B_r B_\phi}{4\pi\rho v_r} \approx \frac{(r\Omega)^2 B_r^2}{4\pi\rho v_r^2}, \quad (35)$$

where Ω is the rotation frequency of a star, B_ϕ is the azimuthal component of the background magnetic field ($B_r B_\phi < 0$ because of winding field lines), and we here consider the problem in the outer region where the super-radial expansion of the flux tubes already finishes, $f = 1$. For the second transformation in Equation (35), we have used the relation for the geometry of magnetic field lines under the steady-state condition,

$$\frac{B_\phi}{B_r} = \frac{v_\phi - r\Omega}{v_r} \approx -\frac{r\Omega}{v_r}, \quad (36)$$

where v_ϕ is the azimuthal component of velocity. If ϵ_B is larger than kinetic energy per mass, the magnetocentrifugal force dominantly works and the wind velocity will be faster than obtained in our simulations. Then, we can use a nondimensional parameter,

$$C_{B\Omega} = \frac{\epsilon_B}{\rho v_r^2/2} = \frac{r^4 B_r^2 \Omega^2}{4\pi r^2 \rho v_r^4/2} = \frac{(B_{r,0} f_0 r_0^2)^2 \Omega^2}{\dot{M} v_r^3/2}, \quad (37)$$

which measures the importance of magnetocentrifugal force⁶. The effect of magnetocentrifugal force becomes important in proportion to magnetic energy and rotation energy but in inversely proportion to a mass loss rate.

We can estimate $C_{B\Omega}$ from a typical case of our simulations for active stars,

$$C_{B\Omega} = 0.57 \left(\frac{B_{r,0} f_0}{5G} \right)^2 \left(\frac{M}{M_\odot} \right) \left(\frac{r_0}{R_\odot} \right) \left(\frac{\dot{M}}{100M_\odot} \right)^{-1} \left(\frac{v_{r,\text{out}}}{400\text{km s}^{-1}} \right)^{-3} \left(\frac{\Omega}{0.1\Omega_K} \right)^2, \quad (38)$$

⁶ What we are doing here is essentially the comparison between the Michel velocity, v_M , (Michel 1969) and the escape velocity, $v_{\text{esc},0}$. Neglecting numerical factors with an order of unity, $C_{B\Omega} = 1$ corresponds to $v_M \approx v_{\text{esc},0}$.

where $\dot{M}_\odot = 2 \times 10^{-14} M_\odot \text{yr}^{-1}$ is the mass loss rate of the current Sun, and $\Omega_K = \sqrt{\frac{GM}{r_0^3}}$ is the Kepler (breakup) velocity at the stellar surface. Equation (38) is normalized by 10 % of Ω_K , which gives the dependences on M and r_0 . The rotation of the current Sun is $\Omega_\odot \approx 0.005\Omega_K$. Then, Equation (37) indicates that the effect of the magnetocentrifugal force is small if the rotation frequency of a star which gives 100 times of \dot{M} is smaller than 20 times of the current solar rotation frequency. In stars with rotation period $\lesssim 1$ day the magnetocentrifugal acceleration is important and the terminal velocity becomes faster, whereas it also depends on the mass loss rate.

6. Summary

We have investigated how the properties of the stellar winds from sun-like stars are determined from the magnetic fields and velocity perturbations at the photosphere. We performed the 163 models of the MHD simulations in the range of ≈ 4 orders of magnitude of the Alfvén wave energy flux from the photosphere. We examined the properties of the stellar winds of these simulations mainly from an energetics point of view. 0.1-10%, with the typical value, $\sim 1\%$, of the input Poynting flux of the Alfvén waves from the photosphere is finally transported to the kinetic energy of the stellar winds. We derived the scaling relations that determine the kinetic energy luminosity and mass loss rate of the stellar winds from the properties at the stellar photosphere (Equations 19, 20, 29 – 32). These relations can be used to estimate the mass losses from solar-type stars (Holzwarth & Jardine 2007; Cranmer & Saar 2011).

We can classify the simulated stellar winds into the unsaturated regime and the saturated regime. When the input wave energies are small, the stellar winds are in the unsaturated state; an increase of the input wave energy directly leads to strong stellar winds. In this regime, the reflection of Alfvén waves dominantly controls the energetics and dynamics of the stellar winds. In the chromosphere and low corona, the density rapidly decreases with height. Consequently, the Alfvén speed rapidly increases, which makes Alfvén waves effectively reflected because of the deformation of the wave shapes. The reflection is more severe for a smaller wave energy input because the density decreases more rapidly without the support from the magnetic pressure ($\propto \delta B_\perp^2/8\pi$) associated with the Alfvén waves. In extreme cases, more than 99% of the input Poynting energies are reflected back before reaching the top of the chromosphere. The mass loss rates of these cases are as small as $\sim 1\%$ of that of the current sun.

With increasing the input wave energy, the density decreases more slowly in the chromosphere owing to the support by the magnetic pressure of the Alfvén waves. The chromosphere of the active cases is time-dependently extended to 10 – 20 % of the radius, and the transition region moves up and down (§5.3) mainly because of the thermally unstable region ($T \gtrsim 10^5$ K) of the radiative cooling function of the gas with the solar abundance (Sutherland

& Dopita 1993). According to the slow decrease of the density in the chromospheres, the Alfvén speed changes more gradually, which suppresses the reflection of the Alfvén waves. When one increases the input wave energy, the kinetic energy and the mass loss rate of the stellar winds increase more rapidly than the linear dependence on the input energy. In cases with the large energy inputs for active stars, more than 10% of the input wave energy from the photosphere reach the top of the chromosphere.

For the large wave energy inputs, the stellar winds are in the saturated state; an increase of the input energy does not raise the kinetic energy of the winds but enhances the radiative loss. Increasing the input wave energy from the unsaturated state to the saturated state, the densities of the transition region and corona monotonically increase, which gives larger kinetic energy and mass loss of the stellar winds. The increase of the densities also raise the radiative cooling. Since the radiative loss is proportional to ρ^2 in the optically thin plasma, the increase of the radiative loss is faster than the increase of the wind kinetic energy with increasing the input wave energy from the photosphere. In the saturated state, most of the Poynting energy at the top of the chromospheres is transferred to the radiation in the transition regions and coronae, and a tiny fraction of the energy is available for the kinetic energy of the stellar winds.

The saturation level has the power-law dependence on $B_{r,0}f_0$, $L_{K,out,sat} \propto (B_{r,0}f_0)^{1.82}$ (Equation 21), which can be understood from the nonlinear dissipation of the Alfvén waves. $B_{r,0}f_0$ determines the magnetic field strength in the upper corona and wind region where the super-radial expansion of the flux tubes already finishes. For small $B_{r,0}f_0$, the nonlinearity of the Alfvén waves, $\delta B_{\perp}/B_r$ becomes systematically larger, which results in faster dissipation. Then, more wave energy dissipates at lower altitudes where the density is higher, and mostly escapes by the radiation loss. For large $B_{r,0}f_0$, the opposite explanation can be done; more wave energy remains up to higher altitudes and contributes to driving the strong stellar winds.

The positive correlation of the saturation level with $B_{r,0}f_0$ indicates that in order to drive strong stellar winds the filling factor of open flux tubes should not be so small, as well as the surface magnetic field should be sufficiently strong. This is consistent with the explanation that closed magnetic loops inhibit stellar winds from active stars. Based on our results, we introduce a speculative scenario for the evolution of the stellar winds from sun-like stars (§5.1; Figure 13). At very early time, the surface of a star is mostly covered with closed magnetic field (small f_0), and then, the mass loss rate is not so large because of the low saturation level, even though the surface field strength ($B_{r,0}$) is large. The magnetic field structure is eventually relaxed so that open flux tubes occupy a larger fraction (f_0 increases) and the mass loss rate increases. After that, the mass loss rate gradually decreases to the current solar level with decreasing magnetic field strength.

Scientific Research from the MEXT of Japan, 22864006. We are grateful to the anonymous referee for many constructive suggestions to improve the paper. We also thank Drs. Brian Wood and Jeffery Linsky for many fruitful discussions. Numerical simulations in this work were partly carried out at the Yukawa Institute Computer Facility, SR16000.

References

- Aarnio, A. N., Matt, S. P., & Stassun, K. G. 2012, *ApJ*, 760: 9
- Alazraki, G. & Couturier, P. 1971, *A&A*, 13, 380
- Anderson, C. S. & Athay, R. G. 1989, *ApJ*, 336, 1089
- Axford, W. I. & McKenzie, J. F. 1997, *The Solar Wind in "Cosmic Winds and the Heliosphere"*, Eds. Jokipii, J. R., Sonnet, C. P., and Giampapa, M. S., University of Arizona Press, 31
- Ayres, T. R. 1997, *J. Geophys. Res.*, 102, 1641
- Belcher, J. W. & MacGregor, K. B. 1976, *ApJ*, 210, 498
- Bogdan, T. J. et al. 2003, *ApJ*, 500, 626
- Brun, A., S., Miesch, M. S., Toomre, J., 2004, 614, 1073
- Carlsson, M. & Leenaarts, J. 2012, *A&A*, 539, A39
- Chandran, B. D. G. 2005 *Phys. Rev. Lett.*, 95, 5004
- Choudhuri, A. R., Schussler, M., & Dikpati, M. 1995, *A&A*, 303, L29
- Cohen, O., Drake, J. J., Kashyap, V. L., Hussain, G. A. J., & Gombosi, T. I. 2010, *ApJ*, 721, 80
- Cranmer, S. R., van Ballegooijen, A. A., Edgar, R. J. 2007, *ApJS*, 171, 520
- Cranmer, S. R. & Saar, S. H. 2011, *ApJ*, 741, 54
- Czesla, S. et al. 2012, *A&A*, 539, 150
- De Moortel, I., Hood, A. W., & Arber, T. D. 2000, *A&A*, 354, 334
- Donati, J.-F. & Collier Cameron, A. 1997, *MNRAS*, 291, 1
- Donati, J.-F. & Landstreet, J. D. 2009, *ARA&A*, 47, 333
- Feulner, G. 2011, *Rev. Geophys.*, 50,
- Fisk, L. A., Schwadron, N. A., & Zurbuchen, T. H. 1999, *J. Geophys. Res.*, 104, A4, 19765
- Fujimura, D. & Tsuneta, S. 2009, *ApJ*, 702, 1443
- Goldstein, M. L. 1978, *ApJ*, 219, 700
- Gondoin, P. 2012, *A&A*, 546, A117
- Gough, D. O. 1981, *Sol. Phys.*, 74, 21
- Grappin, R., Lorat, J., & Buttigheffer, A. 2000, *A&A*, 362, 342
- Gray, D. F. 1992, "The observation and analysis of stellar photospheres", *Cambridge*
- Güdel, M. 2004, *A&A Rev.*, 12, 71 - 237
- Güdel, M. 2007, *Living Rev. Solar Phys.*, 4, 3
- Güdel, M., Guinan, E. F., Skinner, S. L. 1997, *ApJ*, 483, 947
- Hakamada, K., Kojima, M., Ohmi, T., Tokumaru, M., & Fujiki, K. 2005, *Sol. Phys.*, 227, 387
- Heyvaerts, J. & Priest, E. R. 1983, *A&A*, 117, 220
- Hollweg, J. V. 1973, *ApJ*, 181, 547
- Hollweg, J. V. 1984, *Sol. Phys.*, 91, 269
- Holweger, H., Gehlsen, M., & Ruland, F. 1978, *A&A*, 70, 537
- Holzwarth, V. & Jardine, M. 2007, *A&A*, 463, 11
- Hotta, H., Rempel, M., Yokoyama, T., Iida, Y., & Fan, Y., *A&A*, 539, A30
- Hotta, H. & Yokoyama, T. 2011, *ApJ*, 740, 12
- Imada, S., Hara, H., Watanabe, T., Murakami, I., Harra, L. K., Shimizu, T., Zweibel, E. G. 2011, *ApJ*, 743, 57

- Isobe, H., Proctor, M. R. E., & Weiss, N. O. 2008, *ApJL*, 679, L57
- Ito, H., Tsuneta, S., Shiota, D., Tokumaru, M., Fujiki, K. 2010, *ApJ*, 719, 131
- Jacques, S. A. 1977, *ApJ*, 215, 942
- Kahru, J. & Epstein, S. 1986, *Geochim. Cosmochim. Acta*, 50, 1745
- Kasting, J. F. 1997, *Science*, 278, 1245
- Kato, Y., Oskar, S., Matthias, S.; Suematsu, Y. 2011, *ApJL*, 730, L24
- Katsukawa, Y. & Tsuneta, S. 2005, *ApJ*, 621, 498
- Kippenhahn, R. & Weigert, A. 1990 'Stellar structure and evolution', Springer
- Kojima, M., K. Fujiki, M. Hirano, M. Tokumaru, T. Ohmi, and K. Hakamada, 2005, "The Sun and the heliosphere as an Integrated System", G. Poletto and S. T. Suess, Eds. Kluwer Academic Publishers, 147
- Kopp, R. A. & Holzer, T. E. 1976, *Sol. Phys.*, 49, 43
- Kudoh, T., Shibata, K. 1999, *ApJ*, 514, 493
- Lamers, H. J. G. L. M. & Cassinelli, J. P. 1999, 'Introduction to Stellar Wind', Cambridge
- Lammer, H. et al. 2012, *Earth, Planets, and Space*, 64, 179
- Landini, M., Monsignori-Fossi, B.C.: 1990, *A&AS*, 82, 229
- Linsky, J. L., Bushinsky, R., Ayres, T., & France, K. 2012, *ApJ*, 754, 69
- Maggio, A., Sciortino, S., Vaiana, G. S., Majer, P., Bookbinder, J., & Golub, L. 1987, *ApJ*, 315, 687
- Matsumoto, T. & Kitai, R. 2010, *ApJL*, 716, L19
- Matsumoto, T. & Shibata, K. 2010, *ApJ*,
- Matsumoto, T. & Suzuki, T. K. 2012, *ApJ*, 749, 8
- Matt, S. P., MacGregor, K. B., Pinsonneault, M. H., & Greece, T. P. 2012, 754, L26
- Matthaeus, W.H., Zank, G.P., Oughton, S., Mullan, D.J., Dmitruk, P. 1999, *ApJL*, 523, L93
- Michel, F. C. 1969, *ApJ*, 158, 727
- Minton & Malhotra, 2007, *ApJ*, 660, 1700
- Moore, R. L., Suess, S. T., Musielak, Z. E., & An, A.-H. 1991, *ApJ*, 378, 347
- Murawski, K. & Musielak, Z. E. 2010, *A&A*, 518, A37
- Nariyuki Y., Hada, T., & Tsubouchi, K. 2009, *J. Geophys. Res.*, 114, A07102
- Ohyama, M. & Shibata, K. 1998, *ApJ*, 934
- Okamoto, T. J. & De Pontieu, B. 2011, *ApJL*, 736, L24
- Owen, T., Cess, R. D., & Ramanathan, V. 1979, *Nature*, 277, 640
- Pinto, R., Grappin, R., Wang, Y.-M., & Léorat, J. 2009, *A&A*, 497, 537
- Reimers, D. 1975, *Mémoires of the Société Royale des Sciences de Liège*, 8, 369
- Ribas, I., Guinan, E. F., Güdel, M., Audard, M. 2005, *ApJ*, 622, 680
- Rosner, R., Tucker, W. H., & Vaiana, G. S. 1978, *ApJ*, 220, 643
- Saar, S. H. 2001, *the 11th Cool Stars, Stellar Systems and the Sun, ASP Conf. Series*, 223, 292
- Saar, S. H. & Brandenburg, A. 1999, *ApJ*, 524, 295
- Sackmann, I.-J., Boothroyd, A. I., & Kraemer, E. 1993, *ApJ*, 418, 457
- Sackmann, I.-J. & Boothroyd, A. I. 2003, *ApJ*, 583, 1024
- Sagan, C. & Mullen, G. 1972, *Science*, 177, 52
- Schrijver, C. J. & Aschwanden, M. J. 2002, *ApJ*, 566, 1147
- Schröder, K.-P. & Cuntz, M. 2005, *ApJL*, 630, L73
- Shibata, K. & Yokoyama, T. 1999, *ApJL*, 526, L49
- Shibata, K. & Yokoyama, T. 2002, *ApJ*, 577, 422
- Shimojo, M. & Tsuneta, S. 2009 *ApJL*, 706, L145
- Shiota, D., Tsuneta, S., Shimojo, M., Sako, N., Orozco Suárez, D., Ishikawa, R. 2012, *ApJ*, 753, 157
- Skumanich, A. 1972, *ApJ*, 171, 565
- Smith, E. J. & Balogh, A. 2008, *Geophys. Res. Lett.*, 35, L22103
- Sternberg, M. Glenn, Cohen, O., Drake, J. J., Gombosi, T. I. 2011, *J. Geophys. Res.*, A11601271
- Sutherland, R. S. & Dopita, M. A. 1993, *ApJS*, 88, 253
- Suzuki, T. K. 2006, *ApJL*, 640, L75
- Suzuki, T. K. 2007, *ApJ*, 659, 1592
- Suzuki, T. K. 2012, *Earth, Planets, & Space*, 64, 201
- Suzuki, T. K. & Inutsuka, S. 2005, *ApJL*, 632, L49
- Suzuki, T. K. & Inutsuka, S. 2006, *J. Geophys. Res.*, 111, A06101
- Suzuki, T. K., Yan, H., Lazarian, A., & Cassinelli, P. 2006, *ApJ*, 640, 1005
- Telleschi, A. Güdel, M., Briggs, K., Audard, M., Ness, J.-U., Skinner, S. L. 2005, *ApJ*, 622, 653
- Terada, N., Kulikov, Y. N., Lammer, H., Lichtenegger, H. I. M., Tanaka, Y., Shinagawa, H., Zhang, T. 2009, *Astrobio.*, 9, 55
- Terasawa, T., Hoshino, M., Sakai, J. I., & Hada, T. 1986, *J. Geophys. Res.*, 91, 4171
- Tsuneta, S. et al. 2008, *ApJ*, 688, 1374
- Tu, C. Y. & Marsch, E. 2001, *A&A*, 368, 1071
- Verdini, A., Grappin, R., & Velli, M. 2012, *A&A*, 538, A70
- Verdini, A., Velli, M. 2007, *ApJ*, 662, 669
- Vidotto, A. A., Opher M., Jatenco-Pereira, V., & Gombosi, T. I. 2009, *ApJ*, 699, 441
- Weber, E. J., Davis, L., Jr. 1967, *ApJ*, 148, 217
- Whitmire, D. P., Doyle, L. R., Reynolds, R. T., Matese, J. J. 1995, *J. Geophys. Res.*, 100, 5457
- Willson, L. A., Bowen, G. H., & Struck-Marcell, C. 1987, *Comments on Mod. Phys.*, Part C – Comments on Astrophys., 12, 17
- Wood, B. E. & Linsky, J. L. 1998, *ApJ*, 492, 788
- Wood, B. E., Müller, H.-R., Zank, G. P., Linsky, J. L. 2002, *ApJ*, 574, 412
- Wood, B. E., Müller, H.-R., Zank, G. P., Linsky, J. L., Redfield, S. 2005, *ApJL*, 628, L143